SERF deletion modifies amyloid aggregation in a mouse model of Alzheimer's disease

E. Stroo[1#], L. Janssen[1#*], O. Sin[1,2], W. Hogewerf[1], M. Koster[3], L. Harkema[3], S.A. Youssef[3,4], N. Beschorner[5], A.H.G. Wolters[6], B. Bakker[1], Lore Becker[7], L Garrett[7,8], Susan Marschall[7], Sabine M Hoelter[7,8,9], Wolfgang Wurst[10,11,12], Helmut Fuchs[7], Valerie Gailus-Durner[7], Martin Hrabe de Angelis[13,14] , A. Thathiah[15,16], F. Foijer[1], B. van de Sluis[3], J. van Deursen[17], M. Jucker[5], A. de Bruin[3,4], E.A.A. Nollen[1*]

[1]European Research Institute for the Biology of Ageing, University of Groningen, University Medical Centre Groningen, The Netherlands

[2]Graduate Program in Areas of Basic and Applied Biology, Instituto de Ciências Biomédicas Abel Salazar, Universidade do Porto, 4050-313 Porto, Portugal

[3]Department of Biomolecular Health Sciences, Faculty of Veterinary Medicine, Utrecht University, The Netherlands

[4]Department of Pediatrics, Molecular Genetics Section, University of Groningen, University Medical Centre Groningen, The Netherlands

[5]Department of Cellular Neurology, Hertie-Institute for Clinical Brain Research, University of Tübingen, Tübingen, Germany.

[6]Department of Biomedical Sciences of Cells and Systems, University Medical Centre Groningen, The Netherlands

[7]Institute of Experimental Genetics, German Mouse Clinic, Helmholtz Zentrum München, German Research Center for Environmental Health (GmbH), Neuherberg, Germany

[8]Institute of Developmental Genetics , Helmholtz Zentrum München, German Research Center for Environmental Health, Neuherberg, Germany

[9]Technische Universität München, Freising-Weihenstephan, Germany

[10]Chair of Developmental Genetics, TUM School of Life Sciences, Technische Universität München, Freising-Weihenstephan, Germany

[11]Deutsches Institut für Neurodegenerative Erkrankungen (DZNE) Site Munich, Munich, Germany

[12]Munich Cluster for Systems Neurology (SyNergy), Adolf-Butenandt-Institut, Ludwig-Maximilians-Universität München, Munich, Germany

[13]Chair of Experimental Genetics, TUM School of Life Sciences, Technische Universität München, Freising, Germany

[14]German Center for Diabetes Research (DZD), Neuherberg, Germany

[15]VIB Center for the Biology of Disease, KU Leuven Center for Human Genetics, University of Leuven, Leuven, Belgium

[16]Department of Neurobiology, University of Pittsburgh Brain Institute, University of Pittsburgh School of Medicine, Pittsburgh, PA USA

[17]Mayo Clinic, United States of America

[#]These authors contributed equally

[*]Corresponding authors: l.l.s.janssen@umcg.nl or e.a.a.nollen@umcg.nl

Keywords: Small EDRK-rich factor 2, SERF, protein aggregation, amyloid-beta, amyloid polymorphisms, developmental delay

Abstract

In age-related neurodegenerative disease, like Alzheimer's and Parkinson's disease, disease-specific proteins become aggregation-prone and form amyloid-like deposits. Depletion of SERF proteins ameliorates this toxic process in worm- and human cell models for disease. Whether SERF modifies amyloid pathology in mammalian brain, however, has remained unknown. Here, we generated SERF2 brain-specific knockout mice which, unlike full body knockout mice, were viable, and showed no major behavioral and cognitive abnormalities. We combined these knockout mice with the APPPS1 mouse model for human amyloid beta aggregation. Using structure-specific amyloid dyes, previously used to distinguish amyloid polymorphisms in human brain, we show that knockout of SERF2 alters the structure of amyloid fibrils and deposits. Moreover, scanning transmission electron microscopy revealed thicker, shorter and more densely packed amyloid in absence of SERF2. Altogether, our data reveal pleiotropic functions of SERF in development and aging and support a function as a modifier of amyloid aggregation in mammalian brain. Our results indicate that single cellular factors like SERF can determine the structural outcome of amyloid aggregation, offering possibilities for polymorphism-based disease interventions.

Introduction

Protein aggregation is a pathological hallmark shared by several age-related neurodegenerative diseases, such as Alzheimer (AD), Parkinson and Huntington disease. The amyloid-like aggregates that accumulate in each of these diseases are composed of disease-specific proteins, i.e., amyloid-beta (Aβ) and tau in AD[1–4] or alpha-synuclein (α-Syn) in Parkinson disease[5]. While the exact molecular mechanisms underlying the disease pathology remain to be elucidated, genetic evidence indicates that these aggregation-prone proteins play a key role in the disease processes. Mutations altering the production, processing and folding of these proteins are sufficient to cause these diseases[6–23]. Mechanisms underlying age-related protein aggregation include protein homeostatic mechanism that appear to decline with age, which are well studied with the underlying idea that boosting these mechanisms could prevent or delay disease[24–27]. In contrast, little is known about cellular mechanisms that drive toxicity and aggregation of aggregation-prone proteins. Inhibiting such driving mechanisms could provide an alternative and complementary approach to treat protein conformational diseases.

Through a genetic screen in *Caenorhabditis elegans* (*C. elegans*), a highly charged cellular protein has been identified that has the capacity to enhance protein toxicity and aggregation of multiple disease-related, aggregation-prone proteins[28]. This peptide was dubbed *mo*difier of *ag*gregation-4 (MOAG-4) and was found to be an ortholog of two human proteins: SERF1A and SERF2. Interestingly, SERF proteins accelerate the aggregation of multiple amyloidogenic proteins *in vitro*, but not non-amyloidogenic proteins[29–31]. This aggregation promoting effect has been accredited to the interaction of a highly positively charged N-terminal segment with segments of the aggregation-prone proteins that are enriched in negatively charged and hydrophobic, aromatic amino acids leading to the disruption of its inter- and intramolecular electrostatic interactions[31–34]. Neutralizing the charge of MOAG-4 and SERF2 in this N-terminal segment is sufficient to suppress their effect on aggregation and to reduce toxicity in *C. elegans* models for polyglutamine and Aβ pathology[34]. In this study, we use the established APPPS1-21 mouse model for Aβ-pathology to investigate whether the removal of

SERF2 also modifies the aggregation of amyloidogenic proteins in the biologically more complex environment of the mammalian brain.

Results

Full-body Serf2 KO results in developmental delay and perinatal lethality in mice

To establish the role of SERF2 *in vivo*, we first ensured SERF2 expression in all major organs, including the brain, and proceeded to generate full-body *Serf2* knockout (KO) mice (Supplemental Figure 1A-C). During an initial cross, using the four homozygous *Serf2* KO animal (*Serf2*$^{-/-}$) and eight heterozygous *Serf2* KO animals (*Serf2*$^{+/-}$) we obtained, only one *Serf2*$^{-/-}$ survived the day of birth compared to 27 *Serf2*$^{+/-}$ and 96 *Serf2* wild-type (*Serf2*$^{+/+}$) mice (Supplemental Table 1). After backcrossing into C57BL/6J background, interbreeding of *Serf2*$^{+/-}$ animals did not result in any viable *Serf2*$^{-/-}$ mice at the time of weaning (Figure 1A, 1B). To determine whether *Serf2*$^{-/-}$ mice died during fetal development, we examined the offspring at multiple developmental stages: embryonic day 13.5, 15.5 and 17.5. In all of the examined embryonic stages we observed the expected Mendelian ratio of genotypes, around 25 % *Serf2*$^{+/+}$ and *Serf2*$^{-/-}$ embryos and around 50 % *Serf2*$^{+/-}$ (Chi Square: E13.5 $p=0.9672$; E15.5 $p= 0.4432$; E17.5 $p=0.7674$), indicating unaltered viability during embryonic development (Figure 1B). At birth (P0), however, all *Serf2*$^{-/-}$ displayed respiratory distress and the majority (5/7) died within 30 minutes of being born. At the time of weaning, the Mendelian ratio was maintained between the *Serf2*$^{+/+}$ and *Serf2*$^{+/-}$ animals, but no *Serf2*$^{-/-}$ mice survived until this stage (Chi Square: P22 $p<0.0001$) . At E13.5, *Serf2* mRNA levels showed a 50 % reduction for *Serf2*$^{+/-}$ and complete KO for *Serf2*$^{-/-}$ compared to *Serf2*$^{+/+}$(One-way ANOVA: *Serf2*$^{+/-}$ and *Serf2*$^{-/-}$ vs *Serf2*$^{+/+}$ $p_{Bon}<0.0001$). No compensatory change in *Serf1* mRNA levels was observed, suggesting they function independently from each other (Figure 1C). A similar ratio in SERF2 expression was also observed on the protein level (Figure 1D).

Further analysis to uncover the cause of this perinatal lethality revealed a reduction in embryo size of *Serf2*$^{-/-}$ compared to *Serf2*$^{+/+}$ and *Serf2*$^{+/-}$ from E15.5 until birth (Two-way ANOVA: E17.5 WT vs KO

p_{bon}<0.05; P0 WT vs ko p_{Bon}<0.0001) (Figure 1E, S1D-E). No differences in size could be observed between *Serf2*$^{+/+}$ and *Serf2*$^{+/-}$ embryos during the embryonic stage leading up to birth (P0). We excluded placental abnormalities, causing impaired transfer of nutrients and oxygen to the embryo, as a cauce for the growth delays[35]. Examination of placenta at all three embryonic stages for microscopic lesions in the placental labyrinth or other changes, revealed no genotype-related pathology of the placenta. The results indicated that the absence of SERF2 in the embryo itself was responsible for the observed growth phenotype. Histological examination of various tissues revealed a developmental delay of approximately one to two days in the organs of E17.5 *Serf2*$^{-/-}$ embryos compared to the previous time points and standard embryonic development[36,37]. This was most prominent in the lungs, through reduced expansion of alveoli and augmented tissue density (Figure 1F), and in the kidneys, by the increased amount of mesenchyme between the tubules and glomeruli (Supplemental Figure S1F). At the time of birth, the lungs of *Serf2*$^{-/-}$ pups displayed a significantly reduced saccular space (t-test: p= 0.0088) (Figure 1G), reflecting insufficient lung expansion and maturation. This phenomenon, called partial fetal atelectasis, seems to explain the observed respiratory distress and is a likely cause of the perinatal lethality in *Serf2*$^{-/-}$ pups.

SERF2 affects growth in a cell-autonomous manner

Given the ubiquitous expression of SERF2 and its overall effect on growth, we examined whether the effect could be cell intrinsic. We generated CRISPR-induced *Serf2*$^{-/-}$ HEK293T clonal cell lines and found that they also display slower proliferation (Figure 2A). Moreover, RNA sequencing analysis of mouse embryonic fibroblasts (MEF) isolated from E13.5 embryos showed a clear enrichment of GO-terms clustered around three closely related biological functions: cell cycle, cell proliferation and cell adhesion (Figure 2B-C). Interestingly, in the cell cycle cluster we observe an overall upregulation of factors driving cell division and downregulation of growth arrest factors in *Serf2*$^{-/-}$ MEFs (Supplemental Table 2). This observation seems in line with a developmental delay phenotype in *Serf2*$^{-/-}$ mice, because it is known that cell proliferation is favored over differentiation in earlier stages of embryonic development compared to later stages[38]. Overall, the cell culture results point towards a cell-autonomous effect of SERF2 and suggest that deletion of *Serf2* delays cell growth. While our

previous study also demonstrated a cell-autonomous function in regulating protein aggregation for MOAG-4, we did not find visible effects of MOAG-4 deletion on the viability or life span of *C. elegans*[28]. Altogether, our results suggest that the perinatal lethality caused by *Serf2* KO is due to the delayed maturation of certain organs. Given the cell-autonomous nature of the effects of SERF2, we aimed to avoid these adverse effects by creating an brain-specific conditional KO model.

Conditional Serf2 KO mice display a reduction in size, but no other structural abnormalities in the brain..

To circumvent the perinatal lethality of full-body *Serf2* KO mice we generated a brain-specific *Serf2* KO mouse model (*Serf2*$^{br-/-}$) by combining our *Serf2*$^{flox/flox}$ mice with the *Sox1-Cre* model[39] (Figure 3A). Brain-specific KO of Serf2 were indeed viable (Chi Square: p= 0.37) (Supplemental Table 3). Analysis of *Serf2* expression on the mRNA in various organs and on the protein level confirmed brain-specific ablation of *Serf2* by *Sox1*-mediated *Cre* expression in our *Serf2*$^{flox/flox}$ mice (t-test WT vs *Serf2*$^{br-/-}$ brain: 1m p=0.0022; 3m p=0.00527) (Figure 3B-C, Supplemental figure 2A). The small traces of S*erf2* expression detected in the brains of the KO mice is most likely due to the presence of cells from non-neuronal lineage in the samples, e.g. cells from circulatory system. In correspondence with the findings from the full-body KO, we did observe an overall reduction in the brain weight of *Serf2*$^{br-/-}$ of around 10% compared to WT (Two-Way ANOVA: Genotype $p < 0.0001$) (Figure 3D). This difference was already present at 1 month of age and remained at least up to the age of 11 months. Both WT and *Serf2*$^{br-/-}$ displayed similar increases in brain weight between 1 and 3 months of age due to ongoing brain maturation (Two-Way ANOVA: Interaction p=0.8951). This suggests that the reduction in brain size takes place during an early stage of brain development, but that these changes do not necessarily alter continued development. Additional histological examination of the brains with hematoxylin-eosin staining revealed no difference in the cell density (Supplemental Figure 2F), nor did we find any evidence of degeneration, apoptosis or necrosis. Apart from the overall reduction in weight, the brains showed no structural abnormalities and the tissue appeared healthy. We also examined the *Sox1-Cre* mice[39] without floxed *Serf2* (*Cre*^{br}) to distinguish between the effects of *Cre* expression and Serf2 KO. The *Cre*^{br} mice also displayed a reduction in brain weight compared to

the WT controls (Two-Way ANOVA: Genotype p=0.0001) (Figure 3E), but overall it was less pronounced than in *Serf2*$^{br-/-}$ animals. Therefore, *Cre* expression may be partially responsible for the observed decrease in brain size. Overall, brain deletion of SERF2 did not affect the viability or structural integrity of the brain.

Brain-specific KO of Serf2 show no major neurological defects

Next, we performed extensive phenotyping of the *Serf2*$^{br-/-}$ to investigate basic neurologic functioning, motor function and behavior (Figure 4). The most prominent difference we observed in our brain-specific KO model was an overall reduction in body weight compared to WT mice, around 8% for females and 15% for males. Additionally, the *Serf2*$^{br-/-}$ mice appeared slightly more agitated as evidenced by the increased tail elevation and defecation in the SHIRPA (Figure 4, basic neurology panel). The *Serf2*$^{br-/-}$ mice were also more likely to refrain from a secondary response in the hot plate test within the test period of 30 seconds, which could indicate altered or retarded thermoreception. However, we cannot exclude that this phenotype was confounded by alterations in other functions. In the tests for motor functions, *Serf2*$^{br-/-}$ mice show a reduced tendency to passive rotation and reduced latency to falling for both sexes. While this could indicate a motor deficit, none of the other motor tests consistently demonstrated a motor defect across sexes and measured parameters. Moreover, behavioral differences may also influence rotarod performance and could, therefore be the basis of the observed difference. In the behavior assays, we observed a clear difference in the open field measures for distance travelled and center time, again indicating a hyper-responsiveness to mild novelty stress. In the other behavioral tests, we also observed some mild differences in certain parameters, such as decreased percentage of spontaneous alternations in the Y-maze, reduced social affinity, altered acoustic startle at specific amplitudes and reduced pre-pulse inhibition, but only at the lowest interstimulus interval. Overall, the latter changes appear less robust and require confirmation in an independent cohort. While the difference in brain and body size is definitely a factor to be considered during further analysis, our extensive phenotyping of *Serf2*$^{br-/-}$ mice revealed no major deficits in neurological or motor function and only revealed some mild behavioral alterations, predominantly a

slight hyper-responsiveness and increased agitation. Therefore, we decided to proceed with this model to investigate the effect of *Serf2*$^{br-/-}$ on Aβ brain pathology.

Brain-specific KO of Serf2 in APPPS1 mice preserves APP levels or Aβ production

Conditional *Serf2* KO mice were crossed with the *APPPS1-21* amyloid (AM) model[40], which contains human transgenes for both APP with the Swedish KM670/671NL mutation and PSEN1 with the L66P mutation. From this cross we obtained four experimental groups: WT, *Serf2*$^{br-/-}$, AM and AM;*Serf2*$^{br-/-}$ (Figure 5A). Upon crossing of the *Serf2*$^{br-/-}$ with the amyloid model, we observed the expected Mendelian ratio for all the genotypes at P22, indicating that the viability of AM mice was not affected by brain-specific KO of *Serf2* (Chi Square: p= 0.37)(Supplemental Table 3). Based on the known progression of Aβ plaque pathology in the AM mice, we selected two age groups for further analysis: before (1 month) and after (3 months) Aβ plaque deposition (Figure 5B). Analysis of the *Serf2* mRNA and protein levels in both age groups showed that *Serf2* expression was not altered by the Aβ pathology (Two-way ANOVA: *Serf2*$^{br-/-}$ and AM;*Serf2*$^{br-/-}$ vs WT 1m p_{bon} <0.001; 3m p_{bon} <0.0001) (Supplemental Figure 2B-C). The *Serf2*$^{br-/-}$ and the AM;*Serf2*$^{br-/-}$ mice again exhibited the reduction in brain weight previously observed with *Serf2*$^{br-/-}$ (Two-way ANOVA: *Serf2*$^{br-/-}$ vs WT both ages p_{bon}<0.01; AM;*Serf2*$^{br-/-}$ vs WT 1m p_{bon}<0.0001; 3m p_{bon}<0.001) (Supplemental Figure 2D). Also, *Cre*^{br}mice again showed a similar, albeit slightly less pronounced reduction in brain size (Supplemental Figure 2E) and hematoxylin-eosin staining revealed no difference in the cell density (Supplemental Figure 2F) or tissue health due to Serf2 KO.

Next, we examined whether the brain KO of *Serf2* affected any of the key components in the Aβ aggregation process, like altering the levels of APP or the production of its cleavage products, $Aβ_{40}$ and $Aβ_{42}$. We determined the expression of human *APP* in WT, *Serf2*$^{br-/-}$, AM and AM;*Serf2*$^{br-/-}$ mice at both 1 and 3 months of age and observed no difference due to brain specific *Serf2* KO (t-test: 1m p=0.9170; 3m p=0.9963) (Supplemental Figure 2G, data from WT and *Serf2*$^{br-/-}$ not included due to lack of APP construct and absence of signal). Western blot analysis confirmed there was also no difference in APP protein levels between AM and AM;*Serf2*$^{br-/-}$ (t-test: 1m p= 0.1157;3m p=0.5908)

(Supplemental Figure 2H and I). Further analysis of $A\beta_{40}$ (Two-way ANOVA: Genotype p=0.8841; Age p<0.0001; Interaction p=0.8841) (Figure 5C) and $A\beta_{42}$ (Two-way ANOVA: Genotype p=0.7006; Age p<0.0001; Interaction p=0.6522) (Figure 5D) showed an increase in concentration between 1 and 3 months, but this was the same in both AM and AM;*Serf2*$^{br-/-}$. Given the variability in the Aβ concentrations at 3 months and the fact that the ratio between these two peptides is known to affect the aggregation process, we also investigated the correlation between these two Aβ levels (Figure 5E). This analysis showed that mice with a high $A\beta_{42}$ concentration display a similarly high $A\beta_{40}$ level, maintaining a comparable $A\beta_{40}$ /$A\beta_{42}$ ratio for both AM and AM;*Serf2*$^{br-/-}$ animals. Similar to previous observations with MOAG-4 in *C. elegans*, this data suggests that SERF2 does not affect the levels of APP and its cleavage products, $A\beta_{40}$ and $A\beta_{42}$.

Serf2 KO alters the amount of Aβ deposits in the brain

We next investigated whether SERF2 affects the Aβ aggregation by performing immunohistological analysis of the Aβ plaque pathology. Initially, we performed a general Aβ staining using the 6E10 antibody directed at the N-terminal amino acid residues 1-16. In accordance with the known progression of Aβ plaque pathology in the amyloid model, we only found Aβ deposits in the 3-month-old AM and AM;*Serf2*$^{br-/-}$ mice. As expected, most plaques were found in the cortex, with some pathology beginning to spread to the hippocampus as well (Supplemental Figure 3A). The Aβ deposits displayed a broad range of sizes, but we found no differences in global morphology between the plaque population found in AM and AM;*Serf2*$^{br-/-}$ (Supplemental Figure 3B-D). Quantification of the 6E10-positive deposits showed a slight increase in AM;*Serf2*$^{br-/-}$ compared to AM, but this just failed to reach statistical significance in the Bonferroni corrected post-hoc comparison (Two-way ANOVA: all 3m non-AM vs AM groups p_{bon} <0.0001; AM vs AM;*Serf2*$^{br-/-}$ p_{bon} =0.063)(Figure 5F, left panel). Given the high variability in plaque load between animals within the same experimental group, we examined whether this variability reflected the previously observed variation in Aβ levels. Unsurprisingly, animals with higher levels of $A\beta_{40}$ (Figure 5F, right panel) and $A\beta_{42}$ (Supplemental Figure 5A) displayed a higher overall plaque load in both groups. More interestingly, our linear regression analysis revealed that AM;*Serf2*$^{br-/-}$ mice tend to have a higher plaque load than AM mice

with similar Aβ levels (Supplemental Table 4). A second Aβ staining with the similar W0-2 antibody, directed at amino acid residues 4-10, displayed a similar slight increase in the amount of plaque deposits in AM;*Serf2*$^{br-/-}$ at 3 months (Two-way ANOVA: all 3m non-AM vs AM groups p_{bon} <0.0001; AM vs AM;*Serf2*$^{br-/-}$ p_{bon} =0.101) (Figure 5G, Supplemental Figure 5B). In fact, a comparison between the 6E10 and the W0-2 staining in individual animals confirmed the similarity between both staining patterns at 3 months (Supplemental Figure 5C, Supplemental Table S4). Interestingly, our detection algorithm also picked up a small increase in the counts of W0-2-positive foci in the 1 month AM;*Serf2*$^{br-/-}$ group (Two-way ANOVA: 1m WT vs AM;*Serf2*$^{br-/-}$ p_{bon} =0.088 ; *Serf2*$^{br-/-}$ vs AM;*Serf2*$^{br-/-}$ p_{bon} =0.081; AM vs AM;*Serf2*$^{br-/-}$ p_{bon} =0.127; all other comparisons p_{bon} >0.999) (Figure 5G, left panel). Closer examination of the microscopic images revealed the identified spots were not extracellular plaques, but were the result of increased levels of W0-2-positive intracellular Aβ staining in AM;*Serf2*$^{br-/-}$ (Supplemental Figure 6A). Some low level intracellular W0-2 and 6E10 staining could also be observed in the other 1-month-old AM mice, but not to the extent that it was picked up by the detection algorithm (Supplemental Figure 6A-B). This would suggest that the deletion of *Serf2* already alters the intracellular accumulation of Aβ prior to plaque deposition in a way that affects antibody binding affinity.

To investigate if SERF2 also affected the amount of Thioflavin-positive fibrils, we performed Thioflavin-S (ThS) staining. Here, we again observed a large variety in the amount of ThS-positive plaques between individual animals, but we found no mean difference between AM and AM;*Serf2*$^{br-/-}$ mice (Two-way ANOVA: all 3m non-AM vs AM groups p_{bon} <0.001) (Figure 5H, left panel). However, further analysis of the correlation between Aβ levels and the amount of ThS-positive plaques revealed that AM mice showed a positive correlation similar to the general Aβ staining, while AM;*Serf2*$^{br-/-}$ mice displayed an inverse relationship (Figure 5H, right panel, Supplemental Table S4). Consequently, a general increase in Aβ deposits does not equate to an increase in ThS-positive amyloid deposition in AM;*Serf2*$^{br-/-}$ mice, as it does in AM mice (Supplemental Figure 5D). Combining the unaltered levels of amyloid beta with changes in numbers of deposits and their affinity for ThS suggests a change in the amyloid aggregation in *Serf2* KO mice.

Knockout of Serf2 changes the plaque composition and fibril structure

Given the differences in the antibody and ThS binding affinity of the Aβ deposits, we decided to explore the composition within the individual plaques in greater detail. To this end we made use of two luminescent conjugated oligothiophenes (LCO), small hydrophobic ligands that bind distinct amyloid structures and can easily be distinguished from each other based on their individual spectral properties[41]. The smallest, qFTAA, has been shown to stain compact, multifilament fibril structures, coinciding with ThT and Congo red staining[41–43]. The larger hFTAA is capable of staining prefibrillar (non-thioflavinophilic) and single fibril aggregates, also stained with 6E10, but not Congo red, ThT or qFTAA[41–43](Figure 6A). Previous studies have shown that by combining LCO dyes it is possible to uncover structural differences in plaque composition, which were shown to be associated with different disease phenotypes in patients[43–45]. An exploratory frequency analysis of the 502nm/588nm intensity ratios plaques in 3-month-old AM and AM;*Serf2*$^{br-/-}$ mice revealed a three-peak pattern in which the middle peak was similarly represented in both groups (Figure 6B, green area). The first peak, however, was predominantly found in AM mice (Figure 6B, red area), while the third peak was mainly detected in AM;*Serf2*$^{br-/-}$ (Figure 6B, blue area). This shift in ratio was also reflected by a difference in the average intensity ratio between AM and AM;*Serf2*$^{br-/-}$ (t-test $p<0.001$) (Figure 6C). This increase in intensity ratio could not be observed in AM;*Cre*^{br} mice (t-test $p=0.6047$) (Figure 6C, insert), indicating that this effect is caused by the *Serf2* KO and unrelated to *Cre* expression. Given the fact that AM;*Cre*^{br} animals also show a decrease in brain weight (~8% reduction in AM;*Cre*^{br} versus ~11% in the AM;*Serf2*$^{br-/-}$*)* but do not show similar change in LCO staining, this suggest that the structural changes are also unrelated to the reduction in brain weight. Next, we examined if the change in the intensity ratio correlated with the slight increase in 6E10-positive deposits we observed in AM;*Serf2*$^{br-/-}$ (Figure 6D). However, the higher average intensity ratio in AM;*Serf2*$^{br-/-}$ mice was not related to this general plaque load nor the number of W0-2- or ThS-positive deposits (Supplemental Figure 5E-F). Further microscopic analysis of low intensity ratio deposits from AM mice showed a plaque with a qFTAA- and hFTAA-positive core and a border that was only stained by hFTAA (Figure 4E, left panels). The high intensity ratio deposits from AM;*Serf2*$^{br-/-}$ mice, on the other hand,

revealed a qFTAA-positive core, but virtually no hFTAA-staining (Figure 6E, right panels), demonstrating the difference in plaque composition reflected by the shift in LCO intensity ratios. Additionally, we visualized the global fibrillar structure of the plaques on a nanometer scale using high resolution, scanning transmission electron microscopy (STEM). Overall, STEM images of plaques from AM;*Serf2*$^{br-/-}$ tended to show more condensed plaques composed of short, thick and densely packed bundles of fibers with little space in between (Figure 6F, right panels). In the AM mice, however, the plaques we observed displayed more loosely packed fibrils (Figure 6F, left panels). Taken together, these findings suggest *Serf2* KO in mice leads to a shift in the Aβ aggregation process, resulting in an altered structural composition of the plaques.

Discussion

Previous studies identified MOAG-4 and its human orthologs SERF1A and SERF2 as modifiers of aggregation of amyloidogenic proteins. In this study, we have demonstrated in cells and mice that SERF2 provides a growth advantage during development. The absence of SERF2 or MOAG-4 in itself does not appear to be lethal in cells, worms or the brain-specific KO mice. Therefore, we postulate that the observed perinatal lethality in the full-body KO mice is a secondary effect of the delay in growth due to insufficient maturation of certain organs at birth, rather than indicating an essential gene function. This appears to be supported by the fact that some pups survived the initial minutes after birth and incomplete penetrance of the lethality in the earliest generations with mixed genetic background. The 129SV genetic background present in these mice is known to have a gestation period that is on average around one day longer than C57/Bl6J mice[46], which could result in improved lung maturation. These findings are also corroborated by another recent study generating SERF2 KO mice[47].

The effects of SERF2 on growth and development can be caused by several mechanisms. These mechanisms include the facilitation by SERF2 of cell proliferation directly or it protecting cells from stressors that create an unfavorable environment for cell division, both of which would slow general growth in caes of SERF2 depletion. In the latter case, we would expect to see an upregulation of stress

pathways or cell cycle arrest proteins inhibiting the cell cycle in *Serf2*$^{-/-}$ cells. Interestingly, the RNA seq analysis of the MEFs from our *Serf2*$^{-/-}$ mice showed the exact opposite. Cell cycle driving factors were upregulated (e.g. cyclins). Whereas, stress signaling and cell cycle inhibiting factors were downregulated (e.g. GADD45 and GAS1). Thus, the *Serf2*$^{-/-}$ cells actually displayed an increased stimulation of cell proliferation mechanisms, which would fit with cells from earlier stages of embryonic development. While the exact endogenous biological function of SERF2 remains unclear, a recent study showed that SERF1a might play a role as an RNA-organizing protein, which localizes to membraneless nuclear organelles, like the nucleolus, under normal physiological conditions. However, under stress conditions, it was shown to migrate to the cytoplasm, where it could drive amyloid toxicity.[48] While there was no compensatory upregulation of SERF1 in response to SERF2 KO and a similar mode of action remains to be demonstrated for SERF2, the region responsible for the RNA-binding properties of SERF1A is highly conserved in MOAG-4 and SERF2[48]. Given the importance of nucleolar disassembly and reassembly in cell cycle control[49,50], a putative RNA-organizing function could explain how SERF2 facilitates cell proliferation but its precise function in cell proliferation remains to be identified. Loss of SERF2s function in development and cell growth, in addition, would have limited impact in non-proliferating, differentiated cells, like the brain's neurons or the cells of adult *C. elegans*, and may explain why we saw no adverse effects in the *moag-4* deletion worms or our adult *Serf2*$^{br-/-}$ mice.

Additionally, we confirmed the ability of SERF2 to modify the Aβ pathology *in vivo* in a mouse model without it changing the overall Aβ levels. This finding is in accordance with the previously observed effects of MOAG-4 on the aggregation of polyglutamine, Aβ and αSyn in *C. elegans*[28]. At 1 month of age, before plaque deposition, we already observe a change in intracellular Aβ accumulation, which resembles the recently reported intracellular, perinuclear accumulation believed to be the precursor for the dense plaque core[51]. We further showed that mice lacking SERF2 were more prone to form Aβ deposits and that the composition of these deposits was structurally different. In AM mice higher levels of Aβ result in an increase in the numbers of Aβ deposits as well as an increase in the number of ThS-positive deposits. AM;*Serf2*$^{br-/-}$ mice, on the other hand, also show an increase in Aβ deposits, but

this did not lead to higher numbers of ThS-positive plaques, indicating an altered dynamic and outcome of amyloid formation. These findings were further corroborated by the LCO spectra, which revealed that the plaques in AM;*Serf2*$^{br-/-}$ mice have a different conformation of pre-fibrillar and fibrillar Aβ compared to AM mice. Finally, STEM imaging also confirmed a globally altered structure of the amyloid fibrils in the plaques.

Amyloid fibrils are formed through a nucleated self-assembly process characterized by a structural conformation to a β-strand secondary structure and the formation of a critical nucleus during the initial oligomerization. The nuclei act as seeds from which the fibrils grow and have been shown to propagate a specific fibril structure[52,53]. In vitro kinetic assays with SERF and MOAG-4 have shown that these peptides accelerate aggregation by acting on the nucleation phase[30,31,33,54]. Recently, we have shown that SERF2 is equally capable to drive amyloid formation of α-Syn and Aβ *in vitro* through a conserved, positively charged region[34]. Meanwhile, another study has demonstrated that binding of the intrinsically disordered protein yeast SERF to α-Syn and Aβ results in fuzzy complexes with heterogeneous structural conformations that are more extended in nature[54]. Intra-molecular electrostatic interactions have also been proven to play a part in the dynamics and structure of the Aβ monomer folding, which is at the basis of nucleus formation. In fact, several of the familial AD mutations located within the Aβ sequence and reported not to affect the Aβ levels, appear to exert their effects by modifying the intra-molecular interactions and monomer folding[16,55–57]. These mutations have been shown to alter the aggregation kinetics, fibril structure and localization of Aβ accumulation and deposition, giving rise to specific disease phenotypes in mice and human patients[14–16,44,55,58–67]. The differences in Aβ pathology between these mutants seem to display some similarities to the changes we observed between our AM and AM;*Serf2*$^{br-/-}$ mice. Together with the *in vitro* findings about the mechanism of SERF2 interaction with aggregation-prone proteins, this would appear to suggest modulation of intra-molecular interactions and altered nucleation as the mechanism for SERF2's effect on aggregation and amyloid formation in our mice.

Interestingly, there is increasing evidence that qualitative, structural properties may be more related to toxicity than the quantity of aggregates and deposits. Recent studies have provided increasing evidence that structural polymorphs are associated with differences in toxicity and different clinical phenotypes in sporadic and familial cases[45,53,68–70]. One recent study even demonstrated that these structural conformations of distinct disease phenotypes could also be detected by differences in the LCO spectra of the plaques and that these spectral properties could, at least partially, be transmitted to a mouse model through seeding[45].

While the effect of familial mutations on the formation of distinct polymorphs has already been explored by others[45,66,67,71], our study provides the first evidence of a single endogenous factor, separate from Aβ and its production pathway, contributing to a structural shift of amyloid pathology in a mammalian system. Further research will be needed to elucidate the exact structural changes at an atomic level and if they affect toxicity and disease progression similarly to what was previously observed in *C. elegans*. This will provide new insights into the structural properties and diversity of disease-protein aggregation, contributing to a better understanding of the variability in disease manifestation and opening up previously unexplored avenues for therapeutic research. In the case of SERF2 specifically, its apparent antagonistic pleiotropy and potentially reduced biological importance in later life could prove interesting with regard to the treatment of age-related neurodegenerative disorders. However, further exploration of SERF2's endogenous function and how it evolves with ageing will be needed to fully assess this mechanism's therapeutic potential.

Materials and methods

Animals

Serf2 knockout mice were generated by introducing *loxP* sites in the *Serf2* gene on either side of exon 2, in accordance with the 'knockout-first' allele design as described by Skarnes and colleagues[72]. Full-body *Serf2* knockout mice were obtained by crossing these floxed mice with 129SV mice expressing *Cre* under the *Hprt* promoter, resulting in the removal of exon 2 by *Cre*-mediated recombination (Figure S1A). Subsequently, these mice with mixed background were backcrossed at least 6 times to a

C57Bl/6J background. Homozygous and heterozygous full-body *Serf2* knockout mice were examined with their wild-type littermates at embryonic day 13.5, 15.5 and 17.5, as well as at the day of birth (P0) and day of weaning (P22).

Heterozygous *Sox1-Cre* mice[39] were backcrossed at least 8 times to a C57BL/6J background. These animals were also used as controls to differentiate between effects of *Cre* expression and Serf2 knockout. To generate the conditional *Serf2* knockout mice, the floxed mice were first crossed with Tg(ACTFLPe)9205Dym (Jackson#003800) mice to flip the FRT site and remove the lacZ and neo cassette. Subsequently, these mice were backcrossed at least 6 times to a C57BL/6J background. Finally, the resulting homozygous *Serf2*$^{flox/flox}$ mice were crossed with the backcrossed *Sox1-Cre* mice, to obtain the brain-specific *Serf2* knockout mice (Figure S3A). The conditional *Serf2* knockout mice were crossed with the APPPS1-21 transgenic mice (APP (KM670/671NL)/PS1(L166P), Rottenburg, Germany) [40]. A final cross between heterozygous APPPS1-21; *Serf2*$^{flox/flox}$ and heterozygous *Sox1-Cre*; *Serf2*$^{flox/flox}$ resulted in four experimental groups of *Serf2*$^{flox/flox}$ mice: *Sox1-Cre*$^{-/-}$; APPPS1-21$^{-/-}$ (WT), *Sox1-Cre*$^{+/-}$; APPPS1-21$^{-/-}$ (*Serf2*$^{br-/-}$), *Sox1-Cre*$^{-/-}$; APPPS1-21$^{+/-}$ (AM) and *Sox1-Cre*$^{+/-}$; APPPS1-21$^{+/-}$ (AM;*Serf2*$^{br-/-)}$ (Figure 2A). All experimental groups were tested at 1 month or 3 months of age. *Serf2*$^{br-/-}$ for behavioral phenotyping resulted from breeding conditional *Serf2* knockout mice with APPPS1 transgenic mice (APP(KM670/671NL)/PS1dE9)[73] and phenotyping started at the age of 9 weeks.

All experiments were approved by the Institutional Animal Care and Use Committee of the University of Groningen (Groningen, The Netherlands) and by the responsible authority of the district government of Upper Bavaria, Germany.

All mice were maintained on a C57BL/6J background and housed in a 12:12 hour light/dark cycle and the animals had ad libitum access to food and water. Genotyping of embryos was performed using tail and yolk sac biopsies. Otherwise, ear biopsies from labelling were used. DNA was purified using prepGEM® Tissue kit according to a protocol adapted from the manufacturer (ZYGEPTI0500, ZyGEM, VWR International BV) and subjected to PCR using the primers listed in Supplemental

Table S5. If not otherwise stated, mice were terminated through CO_2-inhalation and cervical dislocation for subsequent tissue collection.

Embryo processing and histochemistry

Embryos were fixed in 4 % formalin (Kinipath) for a minimum of 24 hours at room temperature. For the pathological analysis, the embryos and their placenta were bisected longitudinally and embedded in paraffin. Using the microm HM 340E (Thermo Scientific) 4 µm sections were cut for the hematoxylin-eosin (HE) staining. The HE sections were incubated at 60 °C for 15 minutes. Next, sections were deparaffinized and rehydrated in xylene (2x), 100 % alcohol (2x), 96 % alcohol, 70 % alcohol and water. HE staining was performed by incubation with hematoxylin for 4 minutes, water for 10 minutes, eosin for 1 minute and water for 10 seconds. After staining all sections were dehydrated in 70 % alcohol, 96 % alcohol, 100 % alcohol (2x) and xylene (2x).

Brain processing

Upon termination, all brains were collected and weighed. From each experimental group three whole brains were collected for HE staining according to the protocol described under embryo processing. HE-stained sections were scanned with the TissueFAXs microscope using 20X objective. Images were processed for nuclei counts using Histoquest software. The remaining brains were divided sagittally. The left hemibrain was prepared for histochemistry and fixed in 4 % paraformaldehyde (PFA) for 48 hours at room temperature on a shaker. Next, the brains were placed in 30 % sucrose for approximately 12 hours. Afterwards, the excess sucrose was removed and hemibrains were frozen in molds with Tissue Tek O.C.T. compound (Sakura, The Netherlands) on dry ice. The right hemibrain was snap frozen in liquid nitrogen and stored at -80°C. This tissue was homogenized using a liquid nitrogen cooled mortar for subsequent protein and RNA analysis.

Quantitative RT-PCR

Total RNA was extracted from snap frozen tissue using TRIzol Reagent (Life Technologies) according to the manufacturers' description. Total RNA quality and concentration were assessed using a NanoDrop 2000 spectrophotometer (Thermo Scientific/Isogen Life Science). cDNA was made from 1,5 µg total RNA with a RevertAid H Minus First Strand cDNA Synthesis kit (Thermo Scientific) using random hexamer primers. Quantitative real-time PCR was performed using a Roche LightCycler 480 Instrument II (Roche Diagnostics) with SYBR green dye (Bio-Rad Laboratories) to detect DNA amplification. Relative transcript levels were quantitated using a standard curve of pooled cDNA solutions. Expression levels were normalized to β-Actin or 18S mRNA levels. The primers for Quantitative PCR used are listed in Supplemental Table S5.

Western Blot analysis

For SERF2 analysis tissues were homogenized in RIPA buffer (50 mM Tris pH 8, 150 mM NaCl, 5mM EDTA, 0.5 % SDS, 0.5 % SDO, 1 % NP-40) with protease inhibitor cocktail (Roche) and incubated on ice for 1 hour, spun down at 13,300 rpm for 30 minutes at 4 °C and the supernatant was collected. Protein measurements were performed using a BCA kit (Pierce) and 150 µg was loaded on a 10-20 % tris/tricine SDS-page gels (Bio-Rad Laboratories) and blotted onto 0,2 µm nitrocellulose membrane (Bio-Rad Laboratories). Membranes were incubated overnight with SERF2 (1/1500, Protein tech) or Actin (1/10 000, MP biomedicals) antibody. Next, the membranes were incubated with anti-mouse or –rabbit secondary antibodies tagged with horseradish peroxidase (1/10 000, Bio-Rad Laboratories) for one hour at room temperature and visualized by chemiluminescence (Amersham ECL prime western blotting detection reagent, VWR).

RNA sequencing

RNA sequencing analysis was performed on three MEF cell lines from *Serf2*$^{-/-}$ mice and four *Serf2*$^{+/+}$ littermate controls. Total RNA was isolated from MEFs using the Qiagen RNeasy isolation kit. Integrity of the RNA based on RIN scores as determined by a Bioanalyzer (Agilent). RNA-sequencing libraries were prepared using TruSeq Stranded Total RNA with Ribo-Zero Human/Mouse/Rat (RS-122-2201; Illumina, CA, USA) according to manufacturers' protocol. Pooled libraries were sequenced

on an Illumina HiSeq 2500 (single-end 50 bp). Reads were aligned to the mouse reference genome (mm10) using a splicing-aware aligner (StarAligner). Aligned reads were normalized to fragments per million (FPM), excluding low abundance genes (mean FPM>1 in at least two samples). The raw count data were pre-processed using the programming language R (3.4.0) [R Core Team, 2016, available online at: www.r-project.org], the program RStudio (1.0.143) [RStudio Team, 2016, available online at: http://www.rstudio.com/] and the EdgeR package (3.18.0) (Robinson et al., 2010). Genes that displayed FPM value >1 in at least two libraries were retained, resulting in a list of 12,808 genes for differential analysis. Differentially expressed (DE) genes between the *Serf2*$^{+/+}$ and *Serf2*$^{-/-}$ MEFs were identified using the EdgeR general linear model approach. After statistical correction for multiple comparisons with the "false discovery rate" (FDR) method (FDR<0.05), a list of 738 DE genes was obtained. DAVID (6.8) was used to perform functional annotation analyses on this gene list and to identify significantly enriched gene ontology (GO) terms [using GOTERM_BP_DIRECT] [74,75]. The connectivity between the enriched GO terms was further examined by determining the amount of associated genes found (AGF) that were shared between two GO terms. The most significant relationships (where a GO term shared > 25 % of the AGF) were mapped in a network using the igraph package (1.0.1). The color of the edges reflects the major node, with the largest amount of AGF, in each relationship. The weight of the edges was determined by the percentage of AGF shared by the minor node in the relationship. We defined three clusters of GO-terms, where multiple minor GO-terms connected to one or two central, major GO-terms. Minor GO-terms always clustered with the major GO-term with whom they shared the strongest connection. One GO term, positive regulation of the apoptotic process, showed no direct relation with one of the major GO-terms and was therefore assigned to the only cluster it had a significant connection with (Figure S2A-B).

Cell culture

Mouse embryonic fibroblasts (MEFs) were isolated from *Serf2*$^{+/+}$, *Serf2*$^{+/-}$ and *Serf2*$^{-/-}$ E13.5 embryos. MEFs were cultured in T75 culture flasks (Greiner Bio-One, 658175), high–glucose Dulbecco's modified Eagle's medium (Gibco), supplemented with 10% fetal bovine serum (Sigma 12133C), 1 % penicillin/streptomycin (Gibco), non-essential amino acids (Gibco) and β-mercaptoethanol at 37°C, 5

% CO_2 and 3 % O_2. E13.5 embryos. Wild-type HEK293T and two independent clonal lines of CRISPR *Serf2* KO mutant HEK 293T cells were cultured in Dulbecco's Modified Eagle Medium (DMEM, Gibco; high glucose, pyruvate, 41966052), supplemented with 10 % Bovine Cow Serum (BCS; Sigma 12133C) and 1 % Penicillin/Streptomycin (Gibco; 10 000 U/mL, 15140122), at 37 °C, 5 % CO_2. For passaging of cells, 0.05 % Trypsin-EDTA (1X), Phenol Red (Invitrogen; 25300-054) was used. Regular mycoplasma tests were performed.

Cell proliferation assay

For the proliferation assay, 200 000 cells of each cell line were plated in triplicate in a standard 12-well plate and incubated inside the IncuCyte Zoom Live-Cell Imaging System (Essen Bioscience) for over 100 hours. The Incucyte system captured phase contrast images with a 10X magnification every 2 hours at nine distinct locations in each well to determine average confluency as a measure of cell growth. The quantification was performed using the IncuCyte Zoom software. The growth experiment was repeated three times. The confluency data of each experiment was normalized by min-max scaling and the average of the three experiments was plotted (solid line) with the standard deviation (dashed lines).

Mouse phenotyping pipeline

30 Serf $^{br-/-}$ (15 male and 15 female mice) and 30 littermate controls (male and female mice) underwent to a neuro-behavioral phenotypic screening pipeline at the German Mouse Clinic[76,77] (see also www.mouseclinic.de). Measurements were taken from weeks 9 to 29 weeks. Experimental groups were assigned according to the genotype of the animals. Metadata for each data point was recorded throughout the measurements. The phenotypic tests were performed according to the standardized protocol as described before[78–83] and available as extended material & methods. Animal numbers may vary depending on the test performed.

ELISA

The ELISA experiments were performed as described previously[84]. Briefly, the frozen brain samples were homogenized in tissue protein extraction reagent (Pierce) supplemented with complete protease inhibitors (Roche), and centrifuged for 1 hour at 430 000 g at 4 °C. The supernatant was used for ELISA. The $A\beta_{40}$ and $A\beta_{42}$ levels were determined by standard sandwich ELISAs using end-specific antibodies (Janssen Pharmaceutical), and the monoclonal JRFc$A\beta_{40}$/28 and JRFc$A\beta_{42}$/26 antibodies as the capture antibodies. Horseradish peroxidase conjugated JRFAβN/25 or JRFAβN/25 were used as the detection antibodies for, respectively, human Aβ or murine Aβ. Samples were loaded in triplicate for each ELISA. The ELISAs were performed in triplicate for the 3-month-old animals and in duplicate for the 1-month-old animals.

Brain immunohistochemistry

To evaluate Aβ-related pathology, the brain was cut in 30 µm thick serial cryostat sections. A series of sections was selected with 300 µm spacing between individual sections and blind-coded, 6 per mouse for the 6E10 and Iba1 antibody and 3 per mouse for W02. Sections were fixed in 4 % PFA for 10 minutes, followed by 20 minutes antigen retrieval in citrate acid (pH 6.0) and 30 minutes in 1 % H_2O_2 in methanol. Next the sections were incubated for 1 hour in 10 % goat or donkey serum, depending on the secondary antibody, and immunolabeled overnight with antibodies against Aβ, and Iba1 (Supplemental Table S6). The sections were washed and incubated with the complementary biotinylated secondary antibody (1/500, Jackson Immunoresearch) for 2 hours. Next, sections were incubated in ABC complex and reacted with diamino-benzidine (0.5 mg/ml H2O with 0.01 % H_2O_2). The stained sections were scanned with the TissueFAXs microscope using 20X objective. All images were analyzed using the Fiji platform of the ImageJ software[85]. For unbiased feature detection we used a single automated script with optimized threshold method and parameters for the complete image set of each staining method.

Thioflavin-S Staining

A 300 μm-spaced series of three blind-coded 30 μm sections were fixed in 4 % PFA for 10 min, followed by incubation in 0.25 % potassium permanganate solution for 15 min, and a bleaching step with 1 % potassium metabisulfite/1 % oxalic acid for 5 min, incubation with 0.02 % Thioflavin-S solution in 50 % ethanol (Sigma T1892) for 8 minutes, rinsed with water between every step. Finally the sections were incubated with 1 μl/ml DAPI. The sections were analyzed as described for the immunostained sections. Stained sections were scanned with the TissueFAXs microscope using 20X objective. Images were processed using Tissuequest software, selecting the cortex for automated analyses.

Luminescent conjugated oligothiophene (LCO) staining

For the Luminescent conjugated oligothiophenes (LCO) stainings, two different LCO variants, qFTAA (quadro-formyl thiophene acetic acid) and hFTAA (hepta-formyl thiophene acetic acid) were used. Blind-coded 30 μm sections were double-stained with qFTAA and hFTAA (2.4 μM qFTAA and 0.77 μM hFTAA in PBS) similar to a previous description (Nyström et al., 2013). Sections were incubated for 30 minutes in the dark at room temperature. Stainings were analyzed on the Zeiss LSM 510 META confocal microscope equipped with an argon 458 nm laser (Carl Zeiss MicroImaging GmbH, Jena, Germany). An 40x objective (oil-immersion, 1.3 NA, Zeiss) was used for spectral imaging of the Aβ deposits. Stacked images were acquired every 10 nm in the emission spectrum between 470 to 695 nm. Locations were selected randomly from the plaque containing regions of the temporal, frontal and occipital cortex. Images were analyzed using Fiji (Schindelin et al., 2012, 2015) and standard computer algorithms to provide a reproducible, unbiased detection of the plaques. First, the stacks of images across the different wavelengths of the spectrum were combined into one image using the Z-projection sum. A threshold was applied to the resulting image using the “Triangle dark” algorithm to automatically identify and delineate the plaques. Partial plaques on the edge of the images and particles smaller than 25 μm^2 were excluded. These settings allowed us to detect over 98 % of all the plaques in the images. The missed plaques were either too small or too low in intensity to be accurately distinguished from the background. Incorrectly identified particles due to (lipofuscin) auto fluorescence were readily identified based on their wavelength intensity profile and visual inspection

and were also excluded from the analysis. We identified between 17-25 plaques in each animal for the spectral intensity measurements. The ratio of the intensity of emitted light at the blue-shifted portion (502 nm) and red-shifted peak (588 nm) was used as a parameter for spectral distinction of different Aβ deposits. These peaks of the spectra were selected to maximize the spectral distinction.

Large-scale STEM (nanotomy)

The scanning transmission electron microscopy (STEM) experiments were adapted from previously described experiments (Kuipers et al., 2015). Briefly, paraffin embedded cortical sections of AM and AM;*Serf2*$^{br-/-}$ were deparaffinized and postfixed with 1 % osmium tetroxide/1.5 % potassium ferrocyanide in 0.1 M sodium cacodylate, dehydrated through ethanol and embedded in EPON (Serva) using a tissue processor (Leica EM TP 709202). Ultrathin sections (80 nm) were cut using the Leica uc7 ultramicrotome and collected on formvar coated cupper grids (electron microscopy sciences, Hatfield, Pennsylvania). A large area scan using Scanning Transmission Detection was made using a Zeiss supra55 SEM with Atlas. STEM detection with a four quadrant STEM detector was used in inverted darkfield mode, at 28 kV with 30 μm aperture at 3.5 mm working distance. All images were recorded at the same scan speed (cycle time 1.5 minute at 3072×2304 pixels). Contrast and brightness were set based on a live histogram. High resolution large-scale STEM images at 2.5 nm pixel size were generated with the external scan generator ATLAS (Fibics, Canada), individual tiles were stitched in VE viewer (Fibics, Canada), exported as a html-file and uploaded to the website www.nanotomy.org.

Statistical analysis

Unless specified otherwise, statistical analysis was performed using Graphpad v7.02. The exact statistical test used for each comparison is specified in the main body of the text, together with the resulting p-values. In the case of multiple comparisons, a post-hoc analysis with Bonferroni correction was performed. Any corrected p-values derived from this post-hoc analysis are indicated in the text as p_{bon}.

Data availability

RNA-seq data have been deposited in the ArrayExpress database at EMBL-EBI (www.ebi.ac.uk/arrayexpress) under accession number E-MTAB-10083. (http://www.ebi.ac.uk/arrayexpress/experiments/E-MTAB-10083)

Nanotomy datasets are open access available via the repository website www.nanotomy.org/PW/temp02/EllenNollen.

[to be deleted] Upon acceptance of this work the data will be open access available, without password. Pending acceptance, the website can only be accessed by collaborators and reviewers

Acknowledgments

All LCOs were kindly provided by K. Peter R. Nilsson, Linköping University, Sweden. Part of the work has been performed in the UMCG Microscopy and Imaging Center (UMIC), sponsored by ZonMW grant 91111.006 and NWO 40-00506-98-9021. We thank Ben Giepmans for advise on EM studies. This project was funded by a Meervoud Grant from NWO (836.09.001) (to E.A.A.N.), a European Research Council (ERC) starting grant (281622 PDControl) (to E.A.A.N.), the Alumni chapter Gooische Groningers facilitated by the Ubbo Emmius Fonds (to E.A.A.N), an Aspasia fellowship from NWO (015.014.005) (to E.A.A.N.) and the German Federal Ministry of Education and Research (Infrafrontier grant 01KX1012) (to M.H.dA).

Author Contributions

E.S., O.S., L.J. and E.A.A. conceptualized the project. E.S., L.J., O.S. and W.H. performed initial sample collection, sample processing and validation experiments verifying the Serf2 KO models and controls. M.K., L.H., S.A.Y. and A.d.B. provided the embryonic morphological and histological assessment. N.B. and M.J. provided the LCO staining and confocal imaging. A.H.G.W. performed the

large-scale STEM imaging. B.B. and F.F. provided assistance in the isolation and RNA seq analysis of the MEFs. A.T. performed western blotting and ELISA measurements for APP and Aβ content. L.G, S.M.H., and W.W. designed, performed, analyzed and interpreted the behavior assays.

B.v.d.S. and J.v.D. generated the initial Serf2KO animals. L.J. performed the data analysis and wrote the manuscript in collaboration with E.S. and E.A.A.

M.H.dA. acquired funding. M.H.dA. and W.W. conceptualized the phenotyping study. V.G-D., H.F. and S.M.H. supervised the mouse phenotyping study and were responsible for project organization; S.M. generated the mouse cohorts for phenotyping. L.B. and L.G. performed the neuro-behavioral tests and analysed and interpreted the data.

Conflict of Interests

The authors declare that they have no conflict of interest.

References

1. Glenner, G. G. & Wong, C. W. Alzheimer's disease: Initial report of the purification and characterization of a novel cerebrovascular amyloid protein. *Biochemical and Biophysical Research Communications* (1984) doi:10.1016/S0006-291X(84)80190-4.

2. Masters, C. L. *et al.* Amyloid plaque core protein in Alzheimer disease and Down syndrome. *Proc Natl Acad Sci U S A* **82**, 4245–4249 (1985).

3. Grundke-Iqbal, I. *et al.* Microtubule-associated protein tau. A component of Alzheimer paired helical filaments. *Journal of Biological Chemistry* **261**, 6084–6089 (1986).

4. Grundke-Iqbal, I. *et al.* Abnormal phosphorylation of the microtubule-associated protein tau (tau) in Alzheimer cytoskeletal pathology. *Proc Natl Acad Sci U S A* **83**, 4913–4917 (1986).

5. Langley, C. H. & Charlesworth, B. *Nature © Macmillan Publishers Ltd 1997 expansion of xenotransplantation*. (1997).

6. Citron, M. *et al.* Mutation of the β-amyloid precursor protein in familial Alzheimer's disease increases β-protein production. *Nature* (1992) doi:10.1038/360672a0.

7. Murrell, J. R., Hake, A. M., Quaid, K. A., Farlow, M. R. & Ghetti, B. Early-Onset Alzheimer Disease Caused by a New Mutation (V717L) in the Amyloid Precursor Protein Gene. *Archives of Neurology* **57**, 885 (2000).

8. Tomiyama, T. *et al.* A new amyloid β variant favoring oligomerization in Alzheimer's-type dementia. *Annals of Neurology* **63**, 377–387 (2008).

9. Borchelt, D. R. *et al.* Familial Alzheimer's Disease–Linked Presenilin 1 Variants Elevate Aβ1–42/1–40 Ratio In Vitro and In Vivo. *Neuron* **17**, 1005–1013 (1996).

10. Haass, C. *et al.* The Swedish mutation causes early-onset Alzheimer's disease by beta-secretase cleavage within the secretory pathway. *Nat Med* **1**, 1291–6 (1995).

11. Suzuki, N. *et al.* An increased percentage of long amyloid β protein secreted by familial amyloid β protein precursor (βAPP717) mutants. *Science (1979)* (1994) doi:10.1126/science.8191290.

12. Duff, K. *et al.* Increased amyloid-β42(43) in brains of mice expressing mutant presenilin 1. *Nature* (1996) doi:10.1038/383710a0.

13. Murayama, O. *et al.* Enhancement of amyloid β 42 secretion by 28 different presenilin 1 mutations of familial Alzheimer's disease. *Neuroscience Letters* **265**, 61–63 (1999).

14. Nilsberth, C. *et al.* The "Arctic" APP mutation (E693G) causes Alzheimer's disease by enhanced Aβ protofibril formation. *Nature Neuroscience* **4**, 887–893 (2001).

15. Miravalle, L. *et al.* Substitutions at Codon 22 of Alzheimer's A Peptide Induce Diverse Conformational Changes and Apoptotic Effects in Human Cerebral Endothelial Cells*. (2000) doi:10.1074/jbc.M003154200.

16. Ni, C.-L., Shi, H.-P., Yu, H.-M., Chang, Y.-C. & Chen, Y.-R. Folding stability of amyloid-β 40 monomer is an important determinant of the nucleation kinetics in fibrillization. *The FASEB Journal* **25**, 1390–1401 (2011).

17. Conway, K. A., Harper, J. D. & Lansbury, P. T. Accelerated in vitro fibril formation by a mutant α-synuclein linked to early-onset Parkinson disease. *Nature Medicine* (1998) doi:10.1038/3311.

18. Narhi, L. *et al.* Both Familial Parkinson's Disease Mutations Accelerate α-Synuclein Aggregation. *Journal of Biological Chemistry* **274**, 9843–9846 (1999).

19. Conway, K. A. *et al.* Acceleration of oligomerization, not fibrillization, is a shared property of both α-synuclein mutations linked to early-onset Parkinson's disease: Implications for pathogenesis and therapy. *Proc Natl Acad Sci U S A* (2000) doi:10.1073/pnas.97.2.571.

20. Ghosh, D. *et al.* The Parkinson's Disease-Associated H50Q Mutation Accelerates α-Synuclein Aggregation *in Vitro*. *Biochemistry* **52**, 6925–6927 (2013).

21. Ghosh, D. *et al.* The Newly Discovered Parkinson's Disease Associated Finnish Mutation (A53E) Attenuates α-Synuclein Aggregation and Membrane Binding. *Biochemistry* **53**, 6419–6421 (2014).

22. Choi, W. *et al.* Mutation E46K increases phospholipid binding and assembly into filaments of human α-synuclein. *FEBS Letters* **576**, 363–368 (2004).

23. Cooper, J. K. *et al.* Truncated N-terminal fragments of huntingtin with expanded glutamine repeats form nuclear and cytoplasmic aggregates in cell culture. *Human Molecular Genetics* (1998) doi:10.1093/hmg/7.5.783.

24. Labbadia, J. & Morimoto, R. I. The Biology of Proteostasis in Aging and Disease. *Annual Review of Biochemistry* **84**, 435–464 (2015).

25. Boland, B. *et al.* Promoting the clearance of neurotoxic proteins in neurodegenerative disorders of ageing. *Nature Reviews Drug Discovery* **17**, 660–688 (2018).

26. Hipp, M. S., Kasturi, P. & Hartl, F. U. The proteostasis network and its decline in ageing. *Nature Reviews Molecular Cell Biology* **20**, 421–435 (2019).

27. Alberti, S. & Hyman, A. A. Biomolecular condensates at the nexus of cellular stress, protein aggregation disease and ageing. *Nature Reviews Molecular Cell Biology* **22**, 196–213 (2021).

28. van Ham, T. J. *et al.* Identification of MOAG-4/SERF as a regulator of age-related proteotoxicity. *Cell* **142**, 601–612 (2010).

29. Pras, A. *et al.* The cellular modifier MOAG-4/SERF drives amyloid formation through charge complementation. *EMBO J* **40**, e107568 (2021).

30. Falsone, S. F. *et al.* SERF Protein Is a Direct Modifier of Amyloid Fiber Assembly. *Cell Reports* **2**, 358–371 (2012).

31. Yoshimura, Y. *et al.* MOAG-4 promotes the aggregation of α-synuclein by competing with self-protective electrostatic interactions. *J Biol Chem* **292**, 8269–8278 (2017).

32. Meyer, N. H. *et al.* Structural Fuzziness of the RNA-Organizing Protein SERF Determines a Toxic Gain-of-interaction. *Journal of Molecular Biology* **432**, 930–951 (2020).

33. Merle, D. A. *et al.* Increased Aggregation Tendency of Alpha-Synuclein in a Fully Disordered Protein Complex. *Journal of Molecular Biology* **431**, 2581–2598 (2019).

34. Pras, A. *et al.* The cellular modifier MOAG-4/SERF drives amyloid formation through charge complementation. *EMBO J* **40**, e107568 (2021).

35. Ward, J. M., Elmore, S. A. & Foley, J. F. Pathology Methods for the Evaluation of Embryonic and Perinatal Developmental Defects and Lethality in Genetically Engineered Mice. *Veterinary Pathology* **49**, 71–84 (2012).

36. Kaufman, M. H. *The Atlas of Mouse Development*. (Elsevier Science, 1992).

37. Kaufman, M. H. & Bard, J. B. L. *The Anatomical Basis of Mouse Development*. (Elsevier Science, 1999).

38. Ciemerych, M. A. & Sicinski, P. Cell cycle in mouse development. *Oncogene* Preprint at https://doi.org/10.1038/sj.onc.1208608 (2005).

39. Takashima, Y. *et al.* Neuroepithelial Cells Supply an Initial Transient Wave of MSC Differentiation. *Cell* **129**, 1377–1388 (2007).

40. Radde, R. *et al.* Abeta42-driven cerebral amyloidosis in transgenic mice reveals early and robust pathology. *EMBO Rep* **7**, 940–6 (2006).

41. Klingstedt, T. *et al.* Synthesis of a library of oligothiophenes and their utilization as fluorescent ligands for spectral assignment of protein aggregates. *Org Biomol Chem* **9**, 8356–70 (2011).

42. Psonka-Antonczyk, K. M. *et al.* Nanoscale Structure and Spectroscopic Probing of Aβ1-40 Fibril Bundle Formation. *Frontiers in Chemistry* (2016) doi:10.3389/fchem.2016.00044.

43. Nyström, S. *et al.* Evidence for Age-Dependent in Vivo Conformational Rearrangement within Aβ Amyloid Deposits. *ACS Chemical Biology* **8**, 1128–1133 (2013).

44. Lord, A. *et al.* Observations in APP bitransgenic mice suggest that diffuse and compact plaques form via independent processes in Alzheimer's disease. *American Journal of Pathology* **178**, 2286–2298 (2011).

45. Rasmussen, J. *et al.* Amyloid polymorphisms constitute distinct clouds of conformational variants in different etiological subtypes of Alzheimer's disease. *Proceedings of the National Academy of Sciences* **114**, 13018–13023 (2017).

46. Murray, S. A. *et al.* Mouse Gestation Length Is Genetically Determined. *PLoS ONE* **5**, e12418 (2010).

47. Cleverley, K. *et al.* A novel knockout mouse for the small EDRK-rich factor 2 (Serf2) showing developmental and other deficits. *Mammalian Genome* **32**, 94–103 (2021).

48. Meyer, N. H. *et al.* Structural fuzziness of the RNA-organizing protein SERF1a determines a toxic gain-of-interaction. *bioRxiv* 713511 (2019) doi:10.1101/713511.

49. Visintin, R. & Amon, A. The nucleolus: the magician's hat for cell cycle tricks. *Current Opinion in Cell Biology* **12**, 372–377 (2000).

50. Leung, A. K. L. *et al.* Quantitative kinetic analysis of nucleolar breakdown and reassembly during mitosis in live human cells. *The Journal of Cell Biology* **166**, 787–800 (2004).

51. Lee, J.-H. *et al.* Faulty autolysosome acidification in Alzheimer's disease mouse models induces autophagic build-up of Aβ in neurons, yielding senile plaques. *Nature Neuroscience* **25**, 688–701 (2022).

52. Petkova, A. T. *et al.* Self-propagating, molecular-level polymorphism in Alzheimer's β-amyloid fibrils. *Science (1979)* (2005) doi:10.1126/science.1105850.

53. Qiang, W., Yau, W.-M., Lu, J.-X., Collinge, J. & Tycko, R. Structural variation in amyloid-β fibrils from Alzheimer's disease clinical subtypes. *Nature* **541**, 217–221 (2017).

54. Meinen, B. A., Gadkari, V. v., Stull, F., Ruotolo, B. T. & Bardwell, J. C. A. SERF engages in a fuzzy complex that accelerates primary nucleation of amyloid proteins. *Proceedings of the National Academy of Sciences* (2019) doi:10.1073/pnas.1913316116.

55. Grant, M. A. *et al. Familial Alzheimer's disease mutations alter the stability of the amyloid-protein monomer folding nucleus.* vol. 104 https://www.pnas.org/content/pnas/104/42/16522.full.pdf (2007).

56. Lazo, N. D., Grant, M. A., Condron, M. C., Rigby, A. C. & Teplow, D. B. On the nucleation of amyloid β-protein monomer folding. *Protein Science* **14**, 1581–1596 (2009).

57. Elkins, M. R. *et al.* Structural Polymorphism of Alzheimer's β-Amyloid Fibrils as Controlled by an E22 Switch: A Solid-State NMR Study. (2016) doi:10.1021/jacs.6b03715.

58. Ovchinnikova, O. Yu., Finder, V. H., Vodopivec, I., Nitsch, R. M. & Glockshuber, R. The Osaka FAD Mutation E22Δ Leads to the Formation of a Previously Unknown Type of Amyloid β Fibrils and Modulates Aβ Neurotoxicity. *Journal of Molecular Biology* **408**, 780–791 (2011).

59. van Nostrand, W. E., Melchor, J. P., Cho, H. S., Greenberg, S. M. & Rebeck, G. W. Pathogenic effects of D23N Iowa mutant amyloid beta -protein. *J Biol Chem* **276**, 32860–6 (2001).

60. Inayathullah, M. & Teplow, D. B. Structural dynamics of the Δe22 (Osaka) familial Alzheimer's disease-linked amyloid β-protein. *Amyloid* **18**, 98–107 (2011).

61. Bugiani, O. *et al.* Hereditary Cerebral Hemorrhage With Amyloidosis Associated With the E693K Mutation of APP. *Archives of Neurology* **67**, 987–995 (2010).

62. Grabowski, T. J., Cho, H. S., Vonsattel, J. P. G., Rebeck, G. W. & Greenberg, S. M. Novel amyloid precursor protein mutation in an Iowa family with dementia and severe cerebral amyloid angiopathy. *Annals of Neurology* **49**, 697–705 (2001).

63. Philipson, O. *et al.* A highly insoluble state of Aβ similar to that of Alzheimer's disease brain is found in Arctic APP transgenic mice. *Neurobiology of Aging* **30**, 1393–1405 (2009).

64. Shimada, H. *et al.* Clinical course of patients with familial early-onset Alzheimer's disease potentially lacking senile plaques bearing the E693Δ mutation in amyloid precursor protein. *Dementia and Geriatric Cognitive Disorders* **32**, 45–54 (2011).

65. Tomiyama, T. *et al.* A Mouse Model of Amyloid β Oligomers: Their Contribution to Synaptic Alteration, Abnormal Tau Phosphorylation, Glial Activation, and Neuronal Loss In Vivo. *Journal of Neuroscience* **30**, 4845–4856 (2010).

66. Lord, A. *et al.* The Arctic Alzheimer mutation facilitates early intraneuronal Aβ aggregation and senile plaque formation in transgenic mice. *Neurobiology of Aging* **27**, 67–77 (2006).

67. Kulic, L. *et al.* Early accumulation of intracellular fibrillar oligomers and late congophilic amyloid angiopathy in mice expressing the Osaka intra-Aβ APP mutation. *Translational Psychiatry* **2**, e183–e183 (2012).

68. Lu, J. X. *et al.* Molecular structure of β-amyloid fibrils in alzheimer's disease brain tissue. *Cell* (2013) doi:10.1016/j.cell.2013.08.035.

69. Cohen, M. L. *et al.* Rapidly progressive Alzheimer's disease features distinct structures of amyloid-β. *Brain* **138**, 1009–1022 (2015).

70. Cohen, E. *et al.* Reduced IGF-1 Signaling Delays Age-Associated Proteotoxicity in Mice. *Cell* **139**, 1157–1169 (2009).

71. Philipson, O. *et al.* The Arctic amyloid-β precursor protein (AβPP) mutation results in distinct plaques and accumulation of N- and C-truncated Aβ. *Neurobiology of Aging* **33**, 1010.e1-1010.e13 (2012).

72. Skarnes, W. C. *et al.* A conditional knockout resource for the genome-wide study of mouse gene function. *Nature* **474**, 337–342 (2011).

73. Borchelt, D. R. *et al.* Familial Alzheimer's Disease-Linked Presenilin 1 Variants Elevate Abeta1-42/1-40 Ratio In Vitro and In Vivo. *Neuron* **17**, 1005–1013 (1996).

74. Huang, D. W., Sherman, B. T. & Lempicki, R. A. Systematic and integrative analysis of large gene lists using DAVID bioinformatics resources. *Nature Protocols* **4**, 44–57 (2009).

75. Huang, D. W., Sherman, B. T. & Lempicki, R. A. Bioinformatics enrichment tools: paths toward the comprehensive functional analysis of large gene lists. *Nucleic Acids Research* **37**, 1–13 (2009).

76. Gailus-Durner, V. *et al.* Introducing the German Mouse Clinic: open access platform for standardized phenotyping. *Nature Methods* **2**, 403–404 (2005).

77. Fuchs, H. *et al.* Understanding gene functions and disease mechanisms: Phenotyping pipelines in the German Mouse Clinic. *Behavioural Brain Research* **352**, 187–196 (2018).

78. Salminen, A. v *et al.* Meis1: effects on motor phenotypes and the sensorimotor system in mice. *Disease models & mechanisms* **10**, 981–991 (2017).

79. André, V. *et al.* Laboratory mouse housing conditions can be improved using common environmental enrichment without compromising data. *PLOS Biology* **16**, e2005019 (2018).

80. Heermann, T. *et al.* Crybb2 Mutations Consistently Affect Schizophrenia Endophenotypes in Mice. *Molecular Neurobiology* **56**, 4215–4230 (2019).

81. Garrett, L., Lie, D. C., Hrabé de Angelis, M., Wurst, W. & Hölter, S. M. Voluntary wheel running in mice increases the rate of neurogenesis without affecting anxiety-related behaviour in single tests. *BMC Neuroscience* **13**, 61 (2012).

82. Hölter, S. M. *et al.* Tests for Anxiety-Related Behavior in Mice. *Current Protocols in Mouse Biology* **5**, 291–309 (2015).

83. Fuchs, H. *et al.* Mouse phenotyping. *Methods* **53**, 120–135 (2011).

84. Huang, Y. *et al.* Loss of GPR3 reduces the amyloid plaque burden and improves memory in Alzheimer's disease mouse models. *Sci Transl Med* **7**, 309ra164 (2015).

85. Schindelin, J. *et al*. Fiji: an open-source platform for biological-image analysis. *Nature Methods* **9**, 676–682 (2012).

Figure legends

Figure 1. Full-body *Serf2*$^{-/-}$ mice display a developmental delay and perinatal lethality. (A) Schematic overview of the crossing scheme with full-body *Serf2*$^{+/-}$ mice and the resulting genotypic composition of the offspring at embryonic and postnatal stage. **(B)** Absolute animal counts for the three genotypes in the offspring at various days of embryonic development(E13.5, E15.5 and E17.5), at birth (P0) and at time of weaning (P22). **(C)** Real time RT-PCR analyses of *Serf1* and *Serf2* RNA levels in E13.5 heads normalized to housekeeping gene beta-actin (n=4/group, mean±SD, One-way ANOVA for each gene, Bonferroni corrected post-hoc comparison between genotypes ***p<0.001). **(D)** Western blot of SERF2 and actin in *Serf2*$^{+/+}$, *Serf2*$^{+/-}$, *Serf2*$^{-/-}$embryos at E13.5 (black arrow indicates SERF2 band). **(E)** Length measurements of *Serf2*$^{+/+}$, *Serf2*$^{+/-}$, *Serf2*$^{-/-}$ embryos at E15.5, E17.5 and P0 (black line = mean, Two-way ANOVA with factors age and genotype, Bonferroni corrected post-hoc comparison for *Serf2*$^{+/-}$ and *Serf2*$^{-/-}$ compared to *Serf2*$^{-/-}$ *p<0.05; ***p<0.001). **(F)** Hematoxylin and eosin stained lung tissue from *Serf2*$^{+/+}$ and *Serf2*$^{-/-}$ pups at P0 (top: *Serf2*$^{-/-}$, bottom: *Serf2*$^{+/+}$, scale bar=500µm, rectangle =5x magnification in right picture, **(G)** Quantification of the saccolar space in lung tissue from *Serf2*$^{+/+}$ and *Serf2*$^{-/-}$ pups at P0 (black line = mean, t-test **p<0.01). For all mouse data panels: *Serf2*$^{+/+}$= black, *Serf2*$^{+/-}$ = dark grey, *Serf2*$^{-/-}$ = light grey.

Figure 2. Cell culture data of *Serf2* KO and control HEK cells and RNA sequencing analysis of mouse embryonic fibroblasts (MEFs) isolated from full-body *Serf2*$^{-/-}$ and control mice. (A) Growth curve of two CRISPR-induced *Serf2*$^{-/-}$ clones of HEK293T versus wild-type HEK293T. (Three replicates measured,full line=replicate average, dashed lines=standard deviation on average) **(B)** Network showing the interconnectivity of enriched GO-terms in RNA sequencing data from *Serf2*$^{-/-}$ and control MEFs. Circle size indicates amount of differentially expressed genes found in each GO-category. Edges were drawn when the minor category shared more than 25 % of its found genes with the major category. Edge color indicates the major category in the relationship. Edge thickness indicates the percentage of found genes shared by the minor category. **(C)** Bar chart indicating the fold change for each GO-term as determined by DAVID. Brackets indicate the three main GO-term clusters defined based on the network in (B).

Figure 3. Brain-specific conditional KO results in reduced brain weight, partially attributed to Cre-expression. (A) Modified targeting strategy used to delete the exon 2 of *Serf2* specifically in the central nervous system. **(B)** Real time RT-PCR analyses of *Serf2* RNA expression in different organs *Serf2*$^{+/+}$ and *Serf2*$^{br-/-}$ female mice at 1 month and 3 months of age. *Serf2* expression was normalized to housekeeping gene beta-actin (all groups n=6, mean ± SEM). **(C)** Quantification of *Serf2* and beta-actin western blot analysis in brain lysates of WT and *Serf2*$^{br-/-}$ female mice at 1 month (both groups n=6, mean ± SEM, t-test **p<0.01). **(D)** Evolution of brain weight in WT and *Serf2*$^{br-/-}$ female mice between 1 and 11 months of age. **(E)** Brain weight of unfloxed WT and CRE^{br} mice between 1 and 11 months of age. For panel E and D: black line = mean, Two-way ANOVA with factors age and genotype, Bonferroni corrected post-hoc for genotype comparison at each age *p_{bon}<0.05, **p_{bon}<0.01, ***p_{bon}<0.001.

Figure 4. Extensive phenotyping of conditional *Serf2* KO mice reveals reduced body weight and some subtle behavioral changes, but no clear neurological or motor function defects. The top panel provides a schematic overview of the complete phenotyping pipeline used and the ages of testing. Mice were used from a separate breeding line, dedicated to behavioral testing. An overview of the test results is grouped in the 4 bottom panels according to the three general modalities investigated: basic neurological functioning, overall motor function and behavior. Graphs show the -log(p-value) for the comparison between WT and *Serf2*$^{br-/-}$ mice for all parameters tested (vertical black line = significance level of 0.05, sex symbols indicate that sex specific analysis of the parameter only revealed a significant difference for sex).

Figure 5. Crossing a conditional *Serf2* KO with an AM background does not affect Aβ levels, but modifies Aβ plaque formation (A) Schematic overview of the cross between brain-specific *Serf2* KO mice and the amyloid model resulting in four experimental groups: WT, *Serf2*$^{br-/-}$, AM and AM;*Serf2*$^{br-/-}$. **(B)** Timeline for the Aβ pathology in the amyloid model and the selected time points for this study. **(C)** $A\beta_{40}$ and **(D)** $A\beta_{42}$ levels in brain lysate from AM and AM;*Serf2*$^{br-/-}$ mice at 1 and 3 months of age as determined by ELISA normalized to total protein content. (black line = mean, t-test between

genotypes at both ages not significant). **(E)** Correlation plot depicting the relationship between $A\beta_{40}$ and $A\beta_{42}$ levels in AM (black) and AM;*Serf2*$^{br-/-}$ (grey) mice at 3 months of age (detailed statistics in Supplemental Table 3). **(F)** Quantification of the Aβ deposits in the region of interest (ROI) of 6E10 immunostained sagittal brain sections from 1- and 3-month-old AM and AM;*Serf2*$^{br-/-}$ mice (black line = mean, One-way ANOVA between genotypes at both ages, Bonferroni corrected post-hoc between AM and AM;*Serf2*$^{br-/-}$ not significant). Right panel: Correlation plot depicting the relationship between $A\beta_{40}$ levels and 6E10 plaque density in AM (black) and AM;*Serf2*$^{br-/-}$ (grey) mice at 3 months of age. **(G)** Quantification of the Aβ deposits in the ROI of W0-2 immunostained sagittal brain sections from 1- and 3-month-old AM and AM;*Serf2*$^{br-/-}$ mice (black line = mean, One-way ANOVA between genotypes at both ages, Bonferroni corrected post-hoc between AM and AM;*Serf2*$^{br-/-}$ not significant). Right panel: Correlation plot depicting the relationship between $A\beta_{40}$ levels and W0-2 plaque density in AM (black) and AM;*Serf2*$^{br-/-}$ (grey) mice at 3 months of age. **(H)** Quantification of the plaque density in the ROI of Thioflavin-S stained sagittal brain sections from 1- and 3-month-old AM and AM;*Serf2*$^{br-/-}$ mice (black line = mean, One-way ANOVA between genotypes at both ages, Bonferroni corrected post-hoc between AM and AM;*Serf2*$^{br-/-}$ not significant). Right panel: Correlation plot depicting the relationship between $A\beta_{40}$ levels and ThS plaque density in AM (black) and AM;*Serf2*$^{br-/-}$ (grey) mice at 3 months of age. In all panels ROI = cortical and hippocampal area; For all dot plots: WT = black, *Serf2*$^{br-/-}$ = light grey , AM = dark grey and AM;*Serf2*$^{br-/-}$ = white; For correlation plots: AM = black and AM;*Serf2*$^{br-/-}$ = grey, detailed statistics in Supplemental Table 3; ***$p<0.001$; **$p<0.01$; *$p<0.05$.

Figure 6. Brain-specific *Serf2* KO alters the structural composition of amyloid plaques. (A) Graph showing the theoretical LCO dye emission spectra for qFTAA, which binds mature Aβ fibrils (blue), and hFTAA, which binds both mature fibrils and prefibrillar Aβ species (red). **(B)** Frequency distribution of the ratio in fluorescence intensity at 502 nm and 588 nm for all amyloid plaques identified by confocal microscopy in AM (blue) and AM;*Serf2*$^{br-/-}$ (red) mice at 3 months of age. Three peak frequency categories were identified: low IR(red), medium IR (green) and high IR (blue) (n=6 mice/genotype). **(C)** Dot plot representing the intensity ratio of all amyloid plaques identified by

confocal microscopy for AM and AM;*Serf2*$^{br-/-}$ mice at 3 months of age (colors represent the IR categories defined in panel B, black circles correspond to the plaques depicted in panel E, black line = mean, t-test ***p<0.001) (n=6 mice/genotype). **(D)** Correlation plot depicting the relationship between 6E10 plaque density in the ROI and the LCO average intensity ratio in AM (black) and AM;*Serf2*$^{br-/-}$ (grey) mice at 3 months of age (ROI = cortical and hippocampal area, detailed statistics in Supplemental Table 3). **(E)** Spectral confocal microscopy images of amyloid plaques in AM and AM;*Serf2*$^{br-/-}$ mice at 3 months of age of double stained with qFTAA and hFTAA (top= fluorescence at 502 nm, middle= fluorescence at 588 nm, bottom=merged image of 502 nm and 588 nm fluorescence, scale bar = 5 μm). **(F)** Scanning transmission electron microscopy pictures of amyloid plaques in the cortex of AM and AM;*Serf2*$^{br-/-}$ mice at 3 months of age (top scale bar 5μm, rectangle = zoomed region in bottom picture, bottom scale bar = 1μm). High-resolution EM images are available via http://www.nanotomy.org.

Figure 1

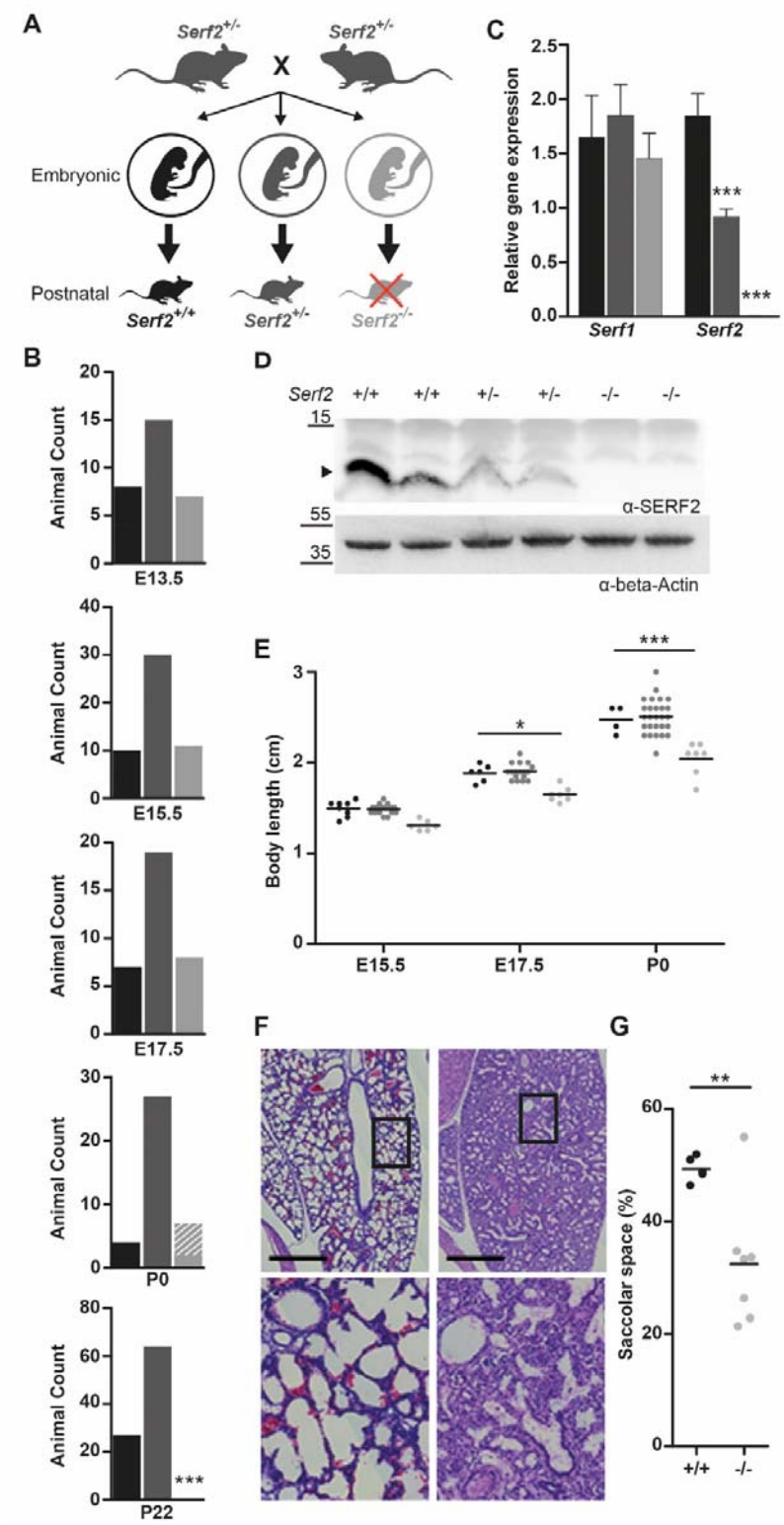
A
Serf2+/-
Serf2+/-
X
Embryonic
Postnatal
Serf2+/+
Serf2+/-
Serf2-/-
C
Relative gene expression
2.5
2.0
1.5
1.0
0.5
0.0
***
***
Serf1
Serf2
B
Animal Count
E13.5
E15.5
E17.5
P0
P22
***
D
Serf2 +/+ +/+ +/- +/- -/- -/-
15
55
35
α-SERF2
α-beta-Actin
E
Body length (cm)
***
*
E15.5
E17.5
P0
F
G
Saccolar space (%)
**
+/+
-/-

Figure 2

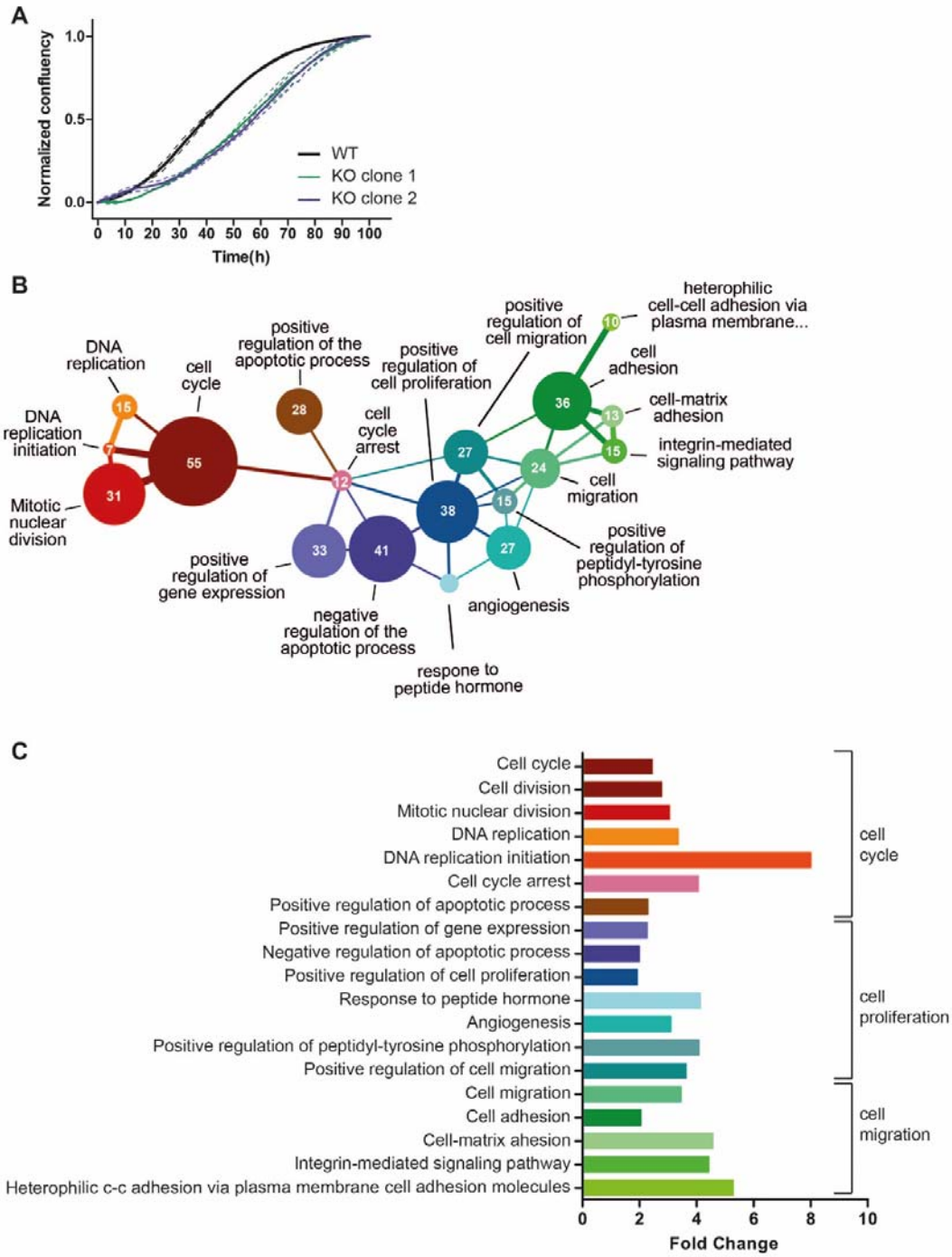
A
Normalized confluency
1.0
0.5
0.0
0 10 20 30 40 50 60 70 80 90 100
Time(h)
WT
KO clone 1
KO clone 2
B
DNA replication
cell cycle
positive regulation of the apoptotic process
positive regulation of cell proliferation
positive regulation of cell migration
heterophilic cell-cell adhesion via plasma membrane...
cell adhesion
cell-matrix adhesion
integrin-mediated signaling pathway
cell migration
DNA replication initiation
Mitotic nuclear division
cell cycle arrest
positive regulation of gene expression
negative regulation of the apoptotic process
respone to peptide hormone
angiogenesis
positive regulation of peptidyl-tyrosine phosphorylation
15
7
31
55
28
12
33
41
38
27
36
10
13
15
24
15
27
C
Cell cycle
Cell division
Mitotic nuclear division
DNA replication
DNA replication initiation
Cell cycle arrest
Positive regulation of apoptotic process
Positive regulation of gene expression
Negative regulation of apoptotic process
Positive regulation of cell proliferation
Response to peptide hormone
Angiogenesis
Positive regulation of peptidyl-tyrosine phosphorylation
Positive regulation of cell migration
Cell migration
Cell adhesion
Cell-matrix ahesion
Integrin-mediated signaling pathway
Heterophilic c-c adhesion via plasma membrane cell adhesion molecules
cell cycle
cell proliferation
cell migration
0 2 4 6 8 10
Fold Change

Figure 3

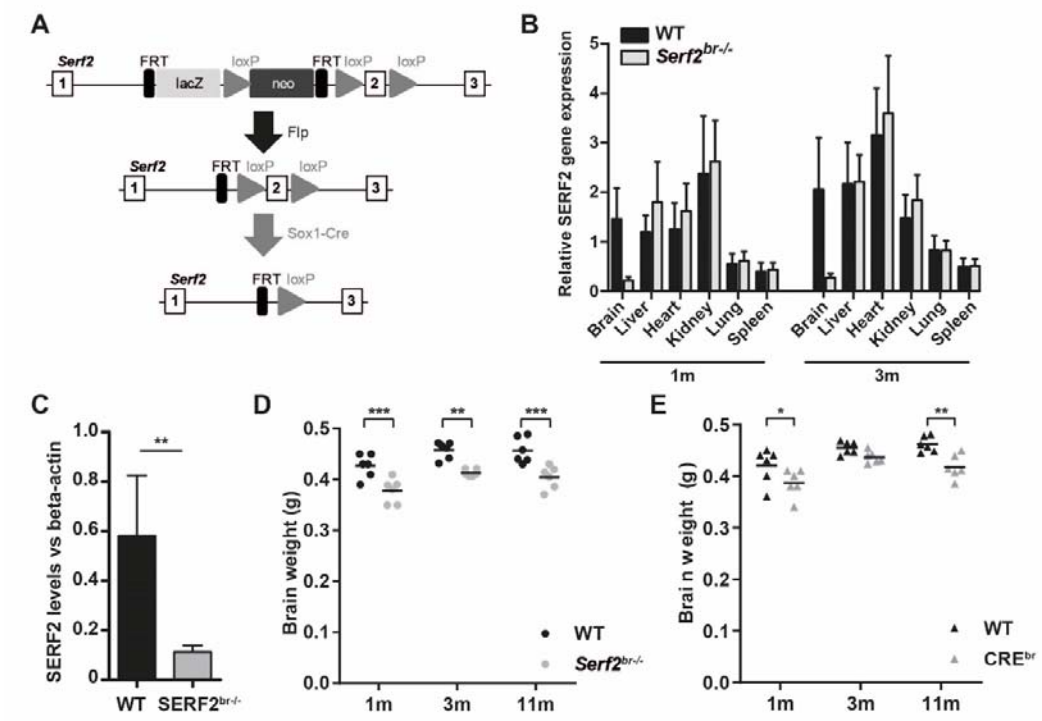
A
Serf2
FRT
lacZ
loxP
neo
FRT
loxP
loxP
1
2
3
Flp
Sox1-Cre
B
WT
Serf2br-/-
Relative SERF2 gene expression
Brain
Liver
Heart
Kidney
Lung
Spleen
1m
3m
C
SERF2 levels vs beta-actin
WT
SERF2br-/-
D
Brain weight (g)
1m
3m
11m
E
Brain weight (g)
CREbr

Figure 4

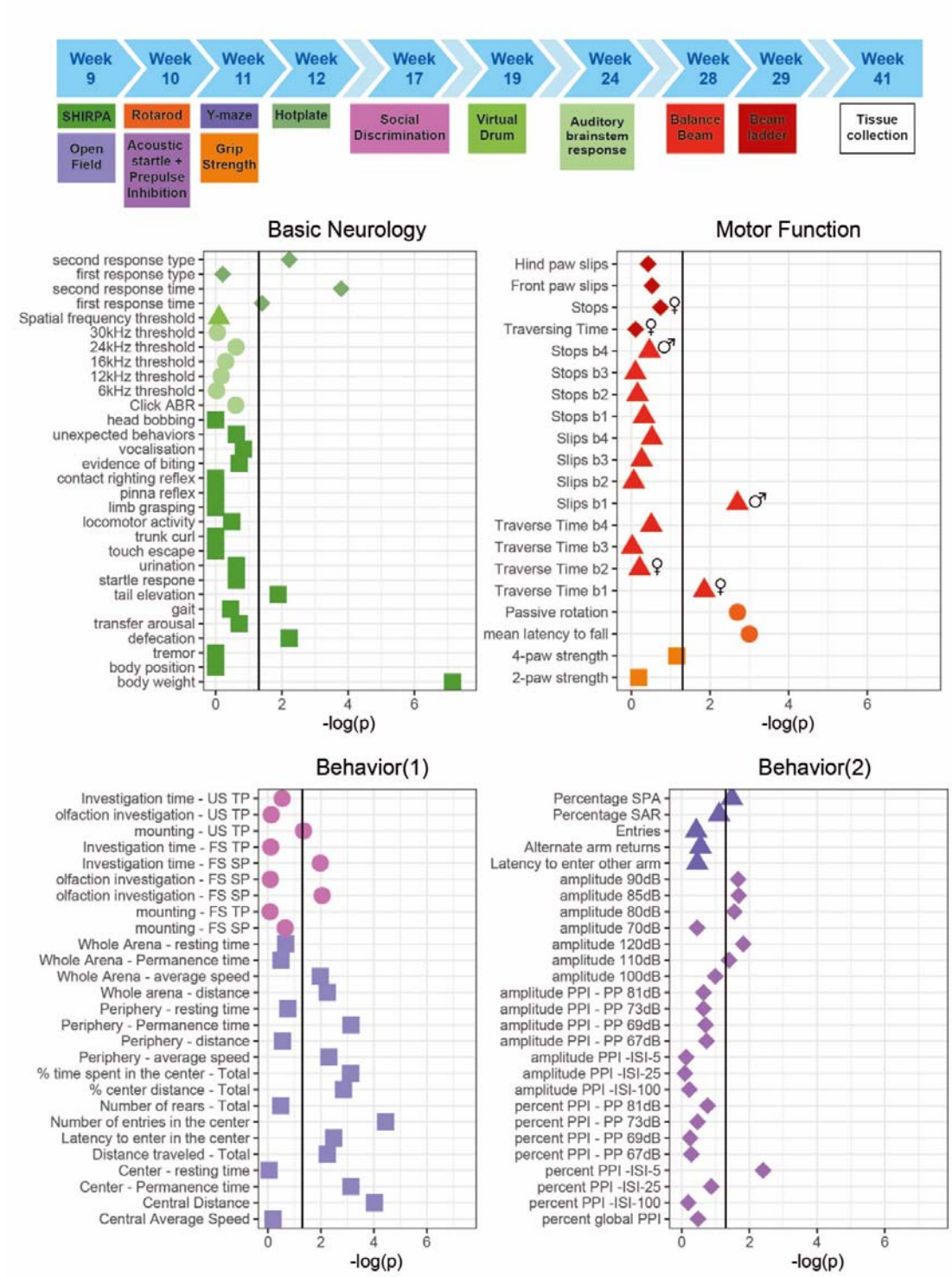
Week 9
Week 10
Week 11
Week 12
Week 17
Week 19
Week 24
Week 28
Week 29
Week 41
SHIRPA
Rotarod
Y-maze
Hotplate
Social Discrimination
Virtual Drum
Auditory brainstem response
Balance Beam
Beam ladder
Tissue collection
Open Field
Acoustic startle + Prepulse Inhibition
Grip Strength
Basic Neurology
second response type
first response type
second response time
first response time
Spatial frequency threshold
30kHz threshold
24kHz threshold
16kHz threshold
12kHz threshold
6kHz threshold
Click ABR
head bobbing
unexpected behaviors
vocalisation
evidence of biting
contact righting reflex
pinna reflex
limb grasping
locomotor activity
trunk curl
touch escape
urination
startle respone
tail elevation
gait
transfer arousal
defecation
tremor
body position
body weight
-log(p)
Motor Function
Hind paw slips
Front paw slips
Stops
Traversing Time
Stops b4
Stops b3
Stops b2
Stops b1
Slips b4
Slips b3
Slips b2
Slips b1
Traverse Time b4
Traverse Time b3
Traverse Time b2
Traverse Time b1
Passive rotation
mean latency to fall
4-paw strength
2-paw strength
-log(p)
Behavior(1)
Investigation time - US TP
olfaction investigation - US TP
mounting - US TP
Investigation time - FS TP
Investigation time - FS SP
olfaction investigation - FS SP
olfaction investigation - FS SP
mounting - FS TP
mounting - FS SP
Whole Arena - resting time
Whole Arena - Permanence time
Whole Arena - average speed
Whole arena - distance
Periphery - resting time
Periphery - Permanence time
Periphery - distance
Periphery - average speed
% time spent in the center - Total
% center distance - Total
Number of rears - Total
Number of entries in the center
Latency to enter in the center
Distance traveled - Total
Center - resting time
Center - Permanence time
Central Distance
Central Average Speed
-log(p)
Behavior(2)
Percentage SPA
Percentage SAR
Entries
Alternate arm returns
Latency to enter other arm
amplitude 90dB
amplitude 85dB
amplitude 80dB
amplitude 70dB
amplitude 120dB
amplitude 110dB
amplitude 100dB
amplitude PPI - PP 81dB
amplitude PPI - PP 73dB
amplitude PPI - PP 69dB
amplitude PPI - PP 67dB
amplitude PPI -ISI-5
amplitude PPI -ISI-25
amplitude PPI -ISI-100
percent PPI - PP 81dB
percent PPI - PP 73dB
percent PPI - PP 69dB
percent PPI - PP 67dB
percent PPI -ISI-5
percent PPI -ISI-25
percent PPI -ISI-100
percent global PPI
-log(p)

Figure 5

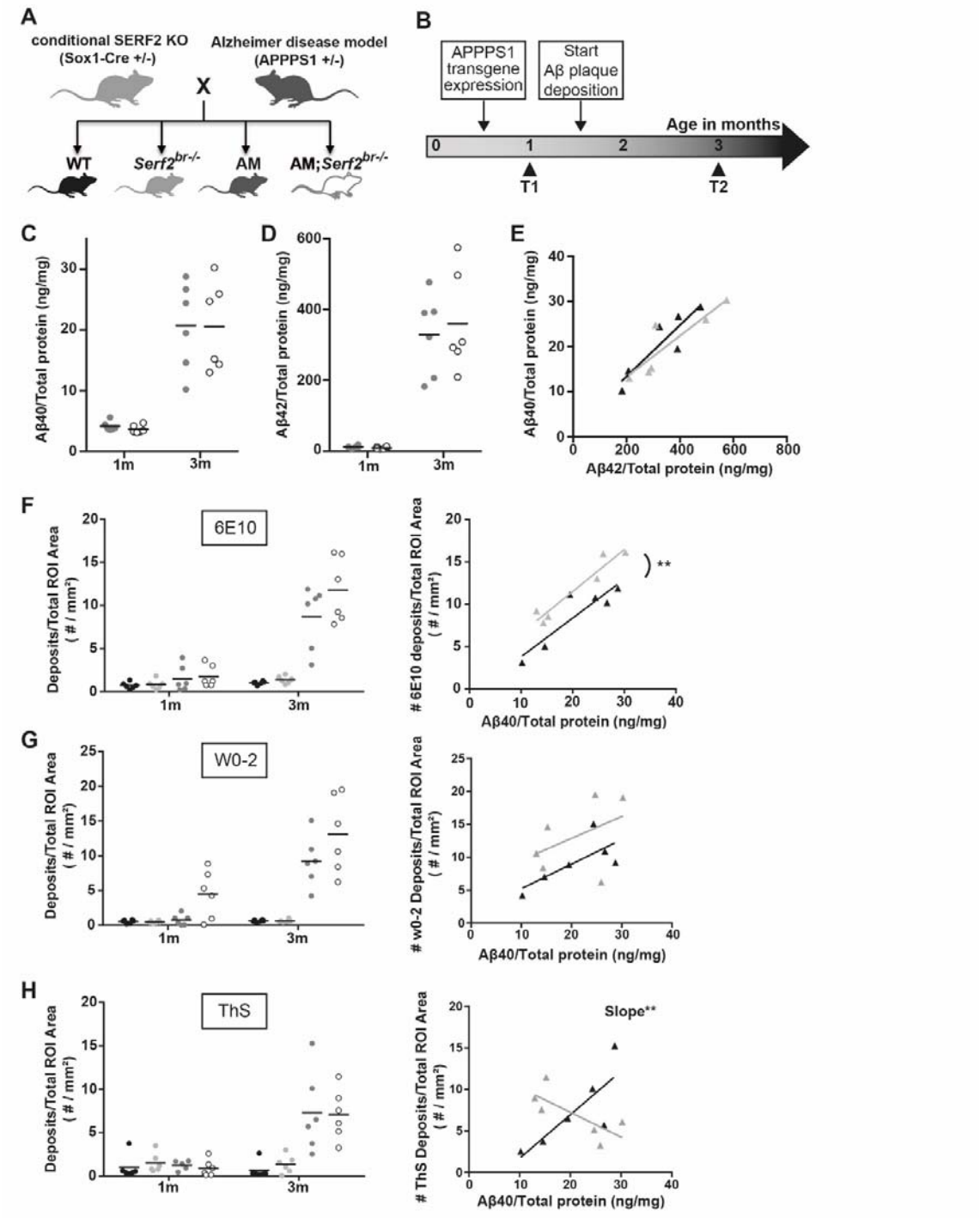
A
conditional SERF2 KO
(Sox1-Cre +/-)
Alzheimer disease model
(APPPS1 +/-)
X
WT
Serf2br-/-
AM
AM;Serf2br-/-
B
APPPS1
transgene
expression
Start
Aβ plaque
deposition
Age in months
0
1
2
3
T1
T2
C
Aβ40/Total protein (ng/mg)
1m
3m
D
Aβ42/Total protein (ng/mg)
E
Aβ40/Total protein (ng/mg)
Aβ42/Total protein (ng/mg)
F
6E10
Deposits/Total ROI Area
(# / mm²)
6E10 deposits/Total ROI Area
(# / mm²)
**
Aβ40/Total protein (ng/mg)
G
W0-2
w0-2 Deposits/Total ROI Area
(# / mm²)
H
ThS
ThS Deposits/Total ROI Area
(# / mm²)
Slope**

Figure 6

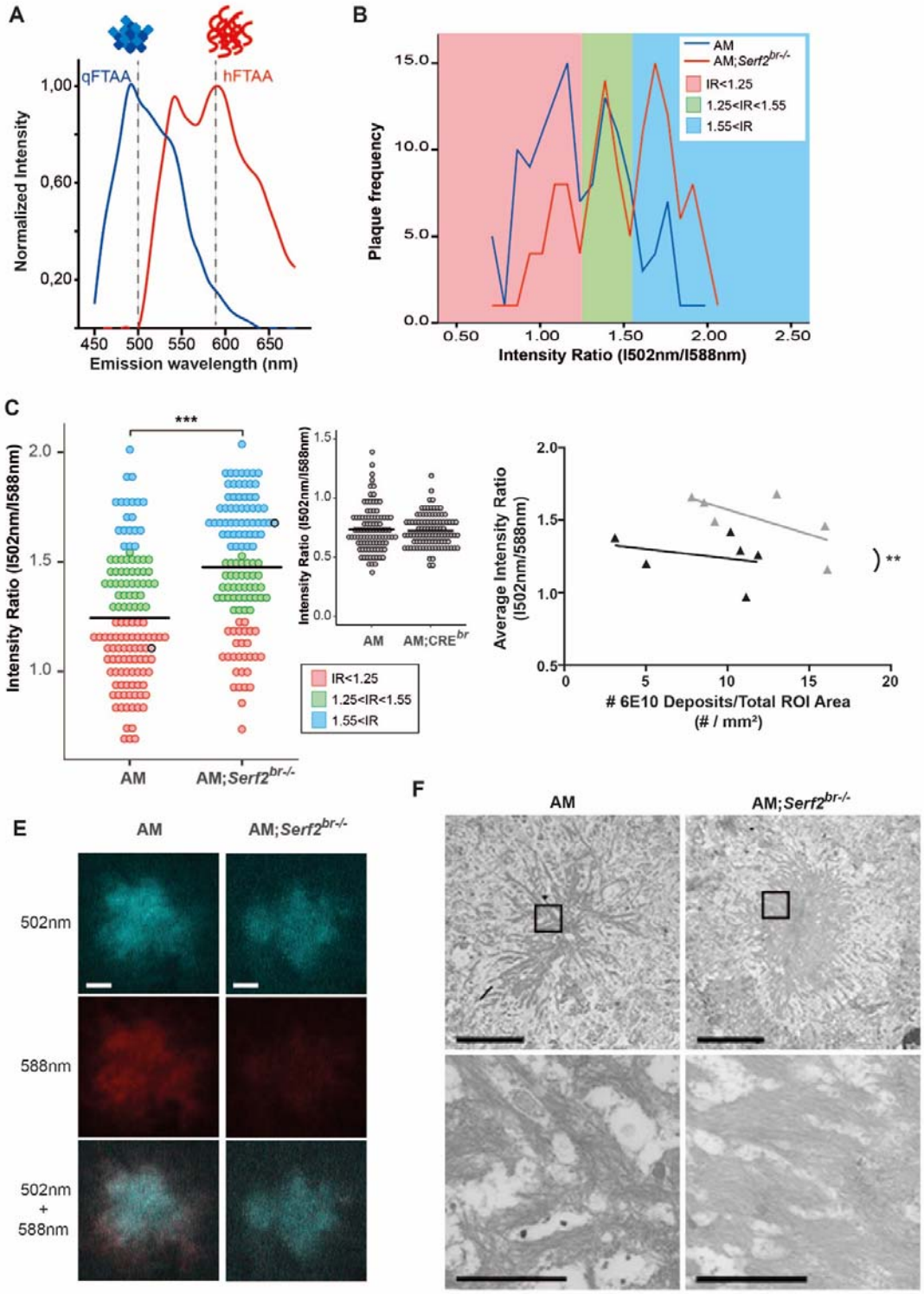
A
qFTAA
hFTAA
Normalized Intensity
1,00
0,60
0,20
450 500 550 600 650
Emission wavelength (nm)
B
AM
AM;Serf2br-/-
IR<1.25
1.25<IR<1.55
1.55<IR
Plaque frequency
15.0
10.0
5.0
0.0
0.50 1.00 1.50 2.00 2.50
Intensity Ratio (I502nm/I588nm)
C
***
Intensity Ratio (I502nm/I588nm)
2.0
1.5
1.0
AM
AM;Serf2br-/-
Intensity Ratio (I502nm/I588nm)
1.5
1.0
0.5
0.0
AM
AM;CREbr
IR<1.25
1.25<IR<1.55
1.55<IR
Average Intensity Ratio (I502nm/588nm)
2.0
1.5
1.0
0.5
0 5 10 15 20
**
6E10 Deposits/Total ROI Area (# / mm²)
E
AM
AM;Serf2br-/-
502nm
588nm
502nm + 588nm
F
AM
AM;Serf2br-/-

Supplemental figure legends

Supplemental Figure 1. Additional full-body *Serf2*$^{-/-}$ mice validation and phenotype confirmation. (A) Targeting strategy used to delete exon 2 of *Serf2* by using the 'knockout-first'-allele (adjusted from Skarnes et al. 2011). Top panel: exon/intron structure of *Serf2* including the positions of the LacZ and Neo cassettes, as well as loxP sites. Bottom panel: the *Serf2* allele after recombination events as a result of crosses with *Hprt-Cre* mice. **(B)** Western blot analysis of liver, heart and brain tissue of a *Serf2*$^{+/+}$, *Serf2*$^{+/-}$ and *Serf2*$^{-/-}$ adult mice to detect Serf2 and actin. **(C)** Real time RT-PCR analyses of *Serf2* in different organs of adult mice with the following genotypes *Serf2*$^{+/+}$ (n=3), *Serf2*$^{+/-}$ (n=8) and *Serf2*$^{-/-}$ (n=1). *Serf2* levels were normalized to the housekeeping gene 18S (mean ± SEM). **(D)** Lateral view of a *Serf2*$^{-/-}$ and *Serf2*$^{+/-}$ embryo and placenta at embryonic day 15.5 and 17.5. **(E)** Weight measurements of *Serf2*$^{+/+}$, *Serf2*$^{+/-}$, *Serf2*$^{-/-}$ embryos at E17.5 and P0 (black line = mean, Two-way ANOVA with factors age and genotype, Bonferroni corrected post-hoc comparison for *Serf2*$^{+/-}$ and *Serf2*$^{-/-}$ compared to *Serf2*$^{-/-}$ *p<0.05; ***p<0.001). **(F)** Hematoxylin and Eosin staining on *Serf2*$^{-/-}$ and *Serf2*$^{+/+}$ lung and kidney tissue at E17.5 (10 times magnification). For all panels: *Serf2*$^{+/+}$= black, *Serf2*$^{+/-}$ = dark grey, *Serf2*$^{-/-}$ = light grey.

Supplemental Figure 2. Basic characterisation of conditional Serf2 KO crossed with an AM background. (A) The western blot of *Serf2* and beta-actin in brain lysates of WT and *Serf2*$^{br-/-}$ female mice at 1 month quantified in main Figure 3 **(B)** Real time RT-PCR analyses of *Serf2* RNA levels in the brain tissue of all experimental groups at 1 and 3 months of age normalized to housekeeping gene beta-actin (n=6/group, mean±SD, Two-way ANOVA with factors age and genotype, Bonferroni corrected post-hoc for individual groups compared to WT). **(C)** Western blot of SERF2 and actin in brain tissue of all experimental groups at 1 and 3 months of age. **(D)** Brain weight of all experimental groups at 1 and 3 months of age (black line = mean, Two-way ANOVA with factors age and genotype, Bonferroni corrected post-hoc for individual groups compared to WT). **(E)** Brain weight of unfloxed control groups at 3 months of age (black line = mean, One-way ANOVA, Bonferroni corrected post-hoc for individual groups compared to WT). **(F)** Number of cortical nuclei per mm^2 in hematoxylin and eosin stained brain tissue of all experimental groups at 3 months of age. (n=3/group, mean±SD,

Kruskal-Wallis p=0.5566). **(G)** Real time RT-PCR analyses of APP RNA levels in the brain tissue of AM and AM;*Serf2*$^{br-/-}$ mice at 1 and 3 months of age normalized to housekeeping gene beta-actin (n=6/group, mean±SD, t-test between genotypes at both ages not significant). **(H)** Western blot of APP and beta-actin in brain tissue of AM and AM;*Serf2*$^{br-/-}$ mice at 3 months of age versus 1-month-old non-AM controls. **(I)** Quantification of total APP protein levels in brains of AM and AM;*Serf2*$^{br-/-}$ mice at 1 and 3 months of age normalized to beta-actin levels. (black line = mean, t-test between genotypes at both ages not significant). In all graphs: WT = black, *Serf2*$^{br-/-}$ = light grey , AM = dark grey and AM;*Serf2*$^{br-/-}$ = white

Supplemental Figure 3. Overview of distribution and general morphological parameters of 6E10-stained Aβ deposits in AM and AM;*Serf2*$^{br-/-}$ mice at 3 months of age. (A) Light microscope images of the 6E10 immunostained sagittal section of 3-month-old AM and AM;*Serf2*$^{br-/-}$ female mice (scale bar = 1mm, black rectangle = region magnified in right panel). **(B)** Boxplots showing the distribution of the surface area of the individual plaques measured in AM and AM;*Serf2*$^{br-/-}$ mice at 3 months of age. **(C)** Boxplots showing the distribution of the circularity of the individual plaques measured in AM and AM;*Serf2*$^{br-/-}$ mice at 3 months of age. **(D)** Boxplots showing the distribution of the solidity of the individual plaques measured in AM and AM;*Serf2*$^{br-/-}$ mice at 3 months of age. For all boxplots: black line = median, box = 25th-75th percentile, whiskers = 1.5 x interquartile range (IQR), circles = outlier value > 1.5x IQR, asterisks = extreme outlier value > 3x IQR.

Supplemental Figure 4. Overview of distribution and detailed W0-2-stained Aβ deposits in AM and AM;*Serf2*$^{br-/-}$ mice at 3 months of age. Light microscope images of the W0-2 immunostained sagittal section of 3-month-old AM and AM;*Serf2*$^{br-/-}$ female mice (scale bar = 1mm, black rectangle = magnified in insert on the right, insert scale bar = 100μm).

Supplemental Figure 5. Correlation plots illustrating the relationship of different stains to Aβ_{42} levels, each other and LCO dyes in individual AM (black) and AM;Serf2br-/- (grey) mice at 3 months of age. (A) Correlation plot depicting the relationship between Aβ_{42} levels and 6E10 plaque density **(B)** Correlation plot depicting the relationship between Aβ_{42} levels and W0-2 plaque density

(C) Correlation plot depicting the relationship between 6E10 and W0-2 plaque density **(D)** Correlation plot depicting the relationship between 6E10 deposits and ThS **(E)** Correlation plot depicting the relationship between W0-2 plaque density and the LCO average intensity ratio **(F)** Correlation plot depicting the relationship between ThS plaque density and the LCO average intensity ratio. For all plots: detailed statistics in Supplemental Table 3; *p <0.05.

Supplemental Figure 6. Overview and detailed view of Aβ staining pattern after W0-2 and 6E10 staining in AM and AM;*Serf2*$^{br-/-}$ mice at 1 month of age. (A) Light microscope images of the W0-2 immunostained sagittal section of 1-month-old AM and AM;*Serf2*$^{br-/-}$ female mice. **(B)** Light microscope images of the 6E10 immunostained sagittal section of 1-month-old AM and AM;*Serf2*$^{br-/-}$ female mice. All pictures: main scale bar = 1mm, black rectangle = magnified in insert on the right, insert scale bar = 100μm.

Supplemental Figure 1

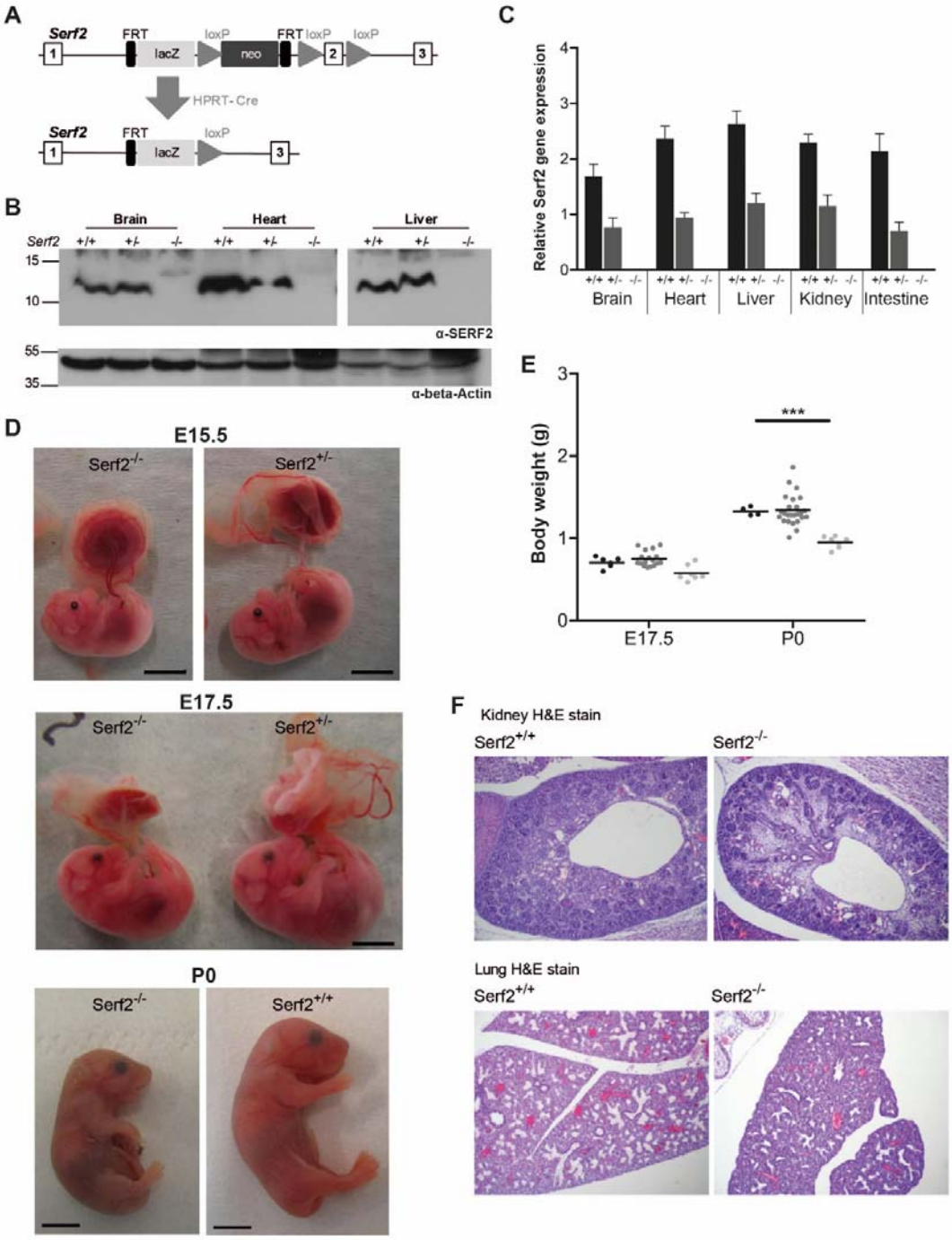

Supplemental Figure 2

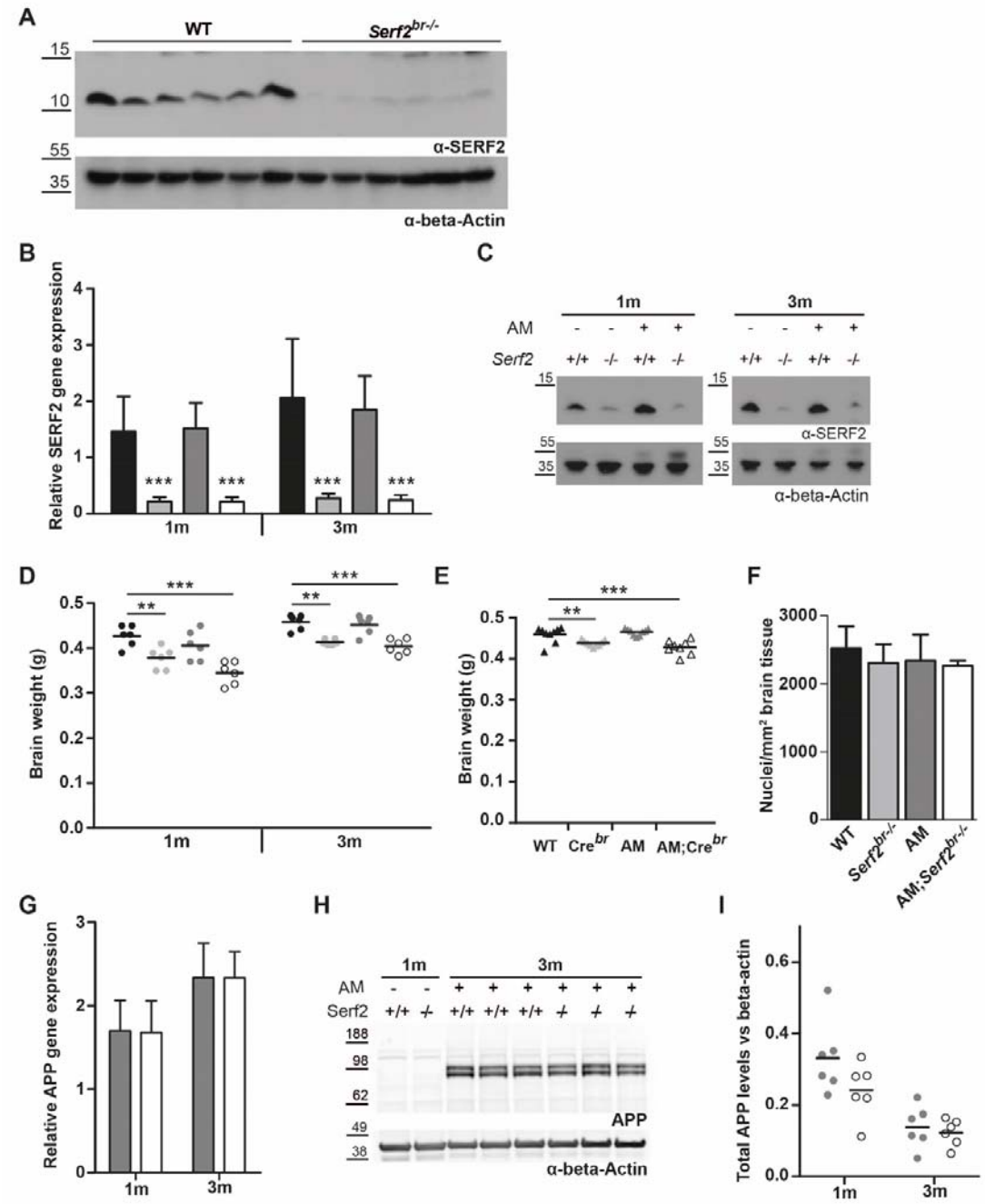

Supplemental Figure 3

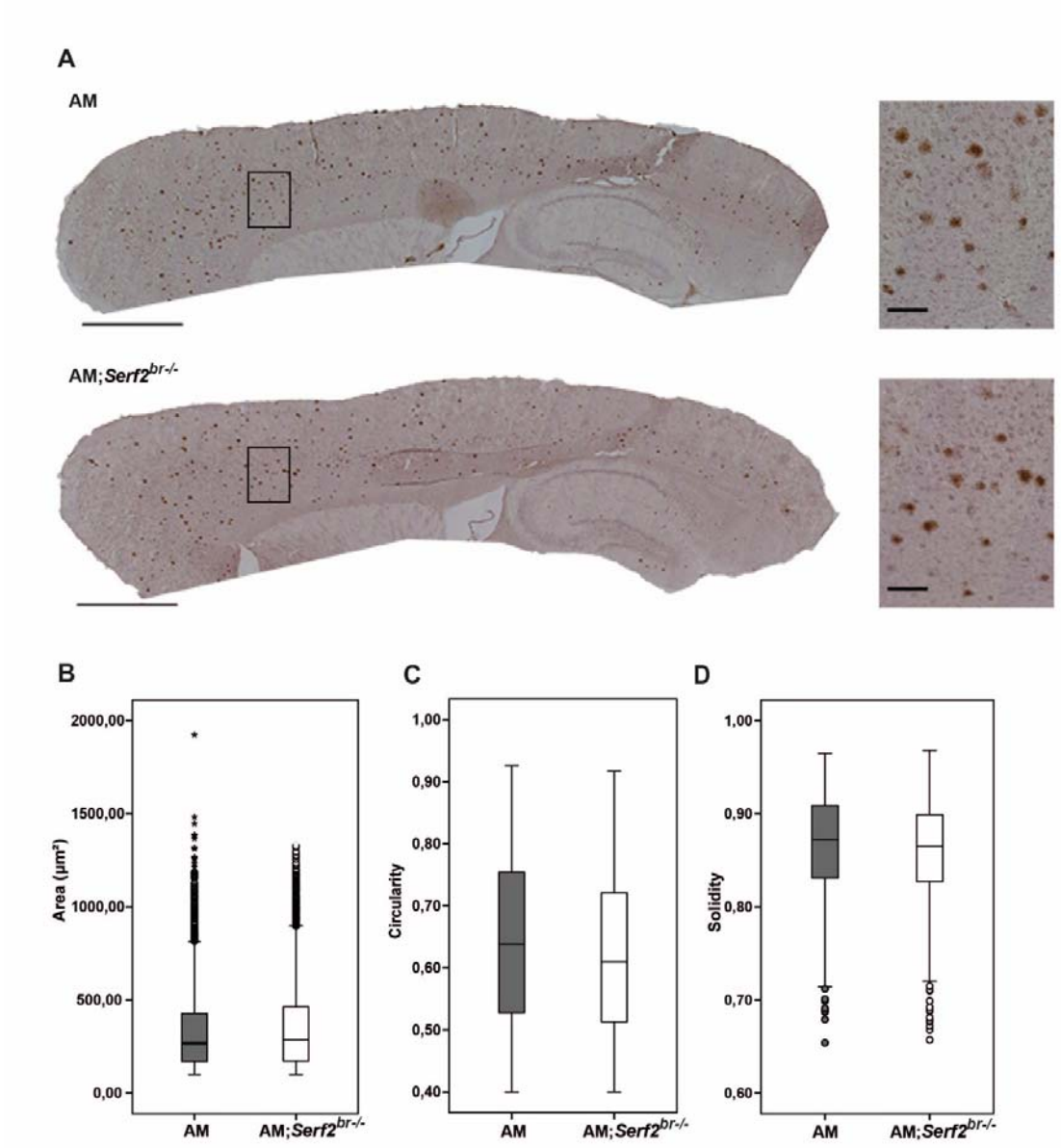

Supplemental Figure 4

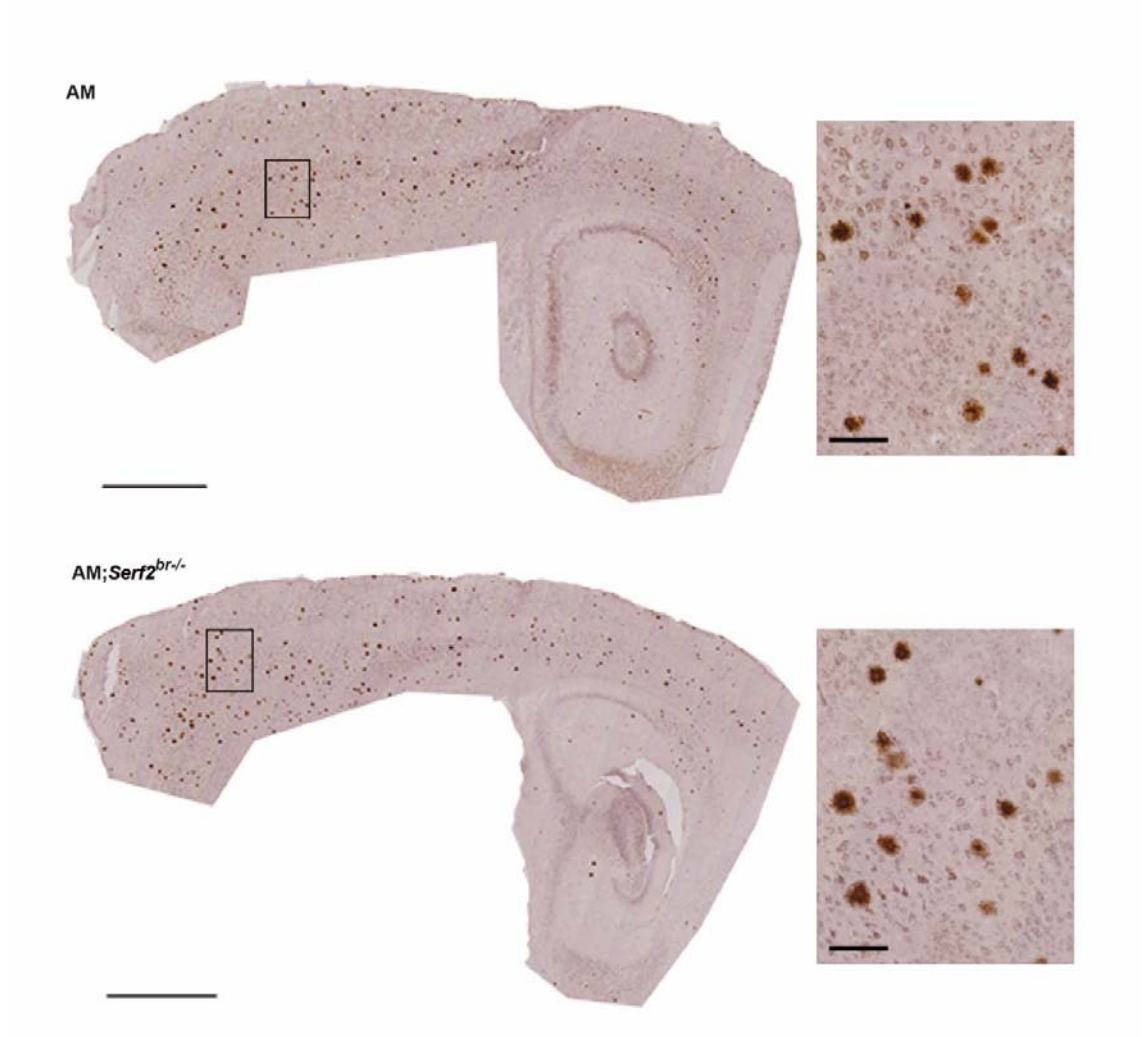

Supplemental Figure 5

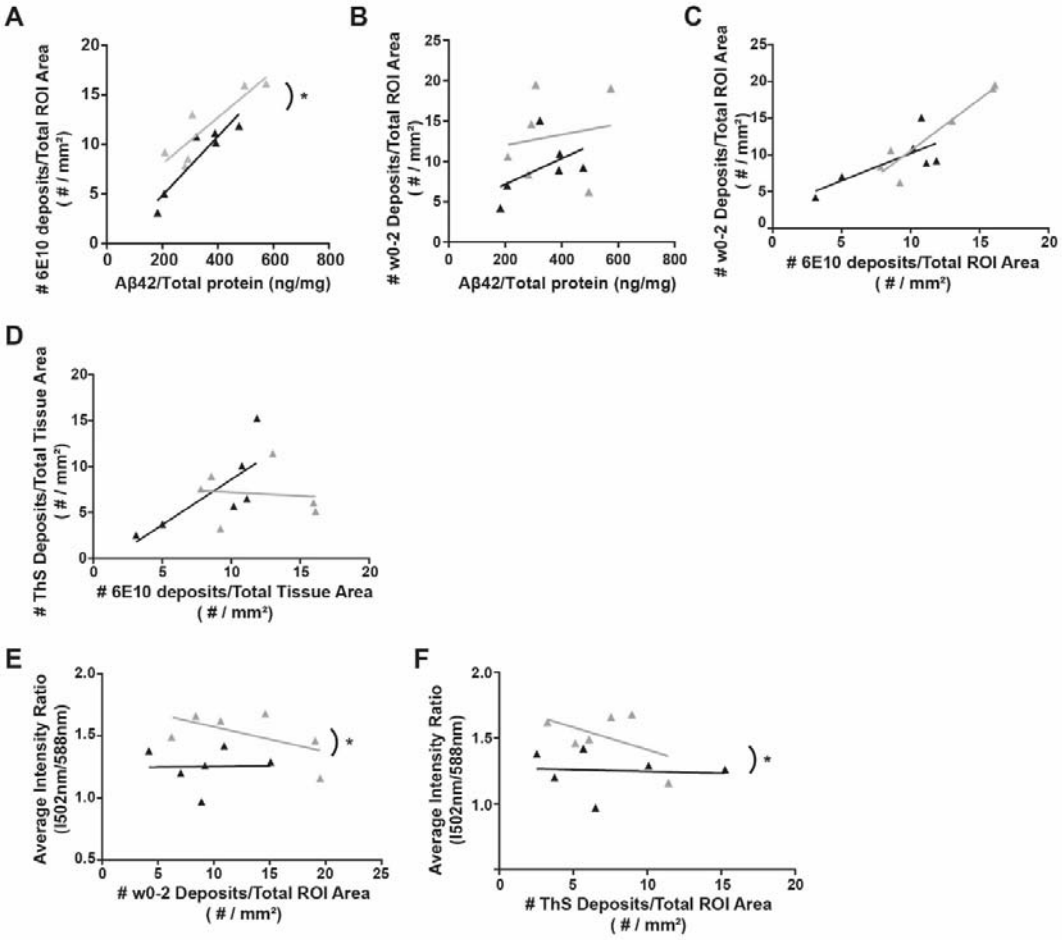
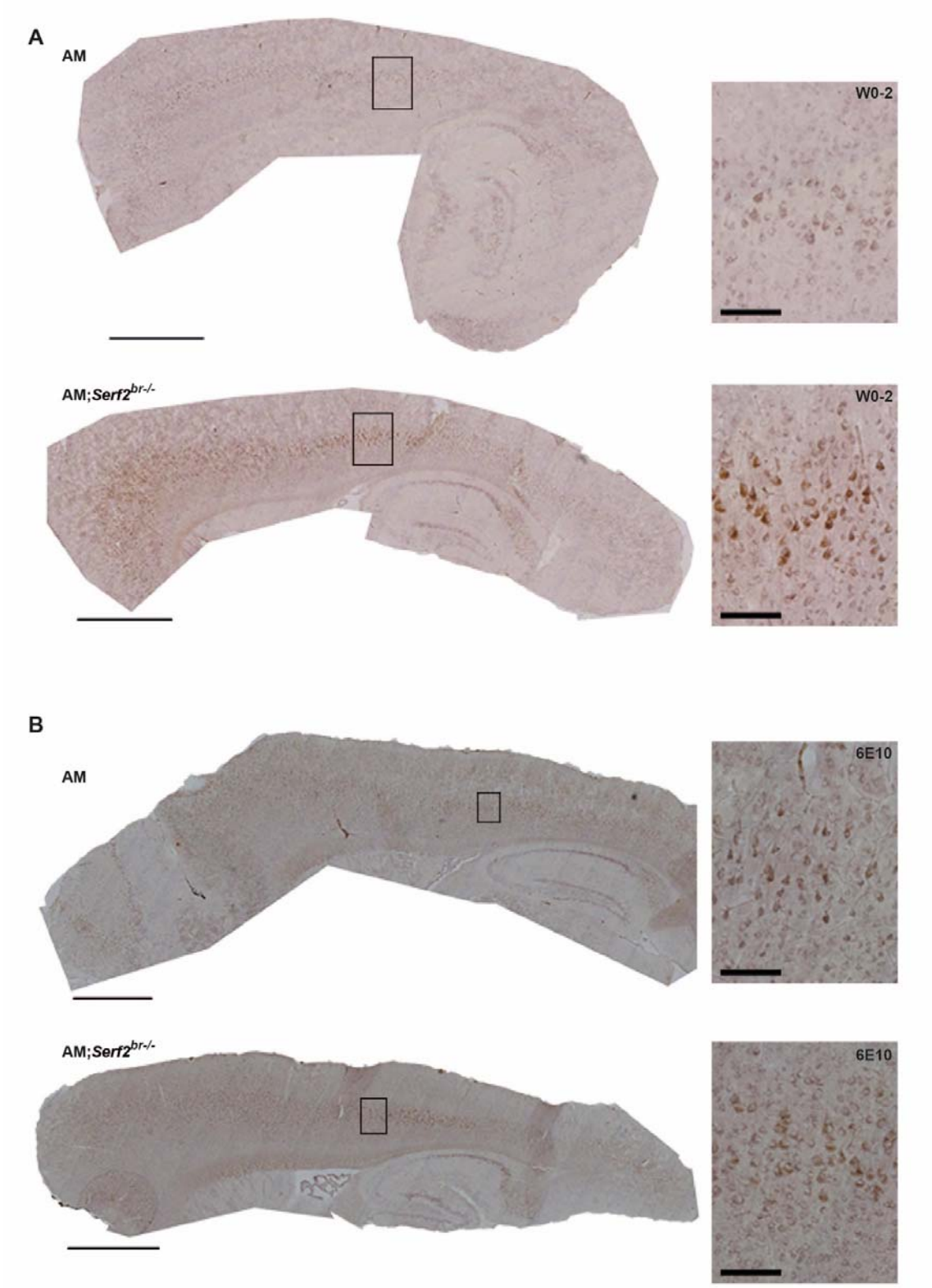
Supplemental Figure 6